

An investigation into the effects of modelling assumptions on sound power radiated from a high-speed train wheelset

Gong Cheng ¹, Yuanpeng He ¹, Jian Han ³, Xiaozhen Sheng ^{2*}, David Thompson ⁴

¹ State Key Laboratory of Traction Power, Southwest Jiaotong University, Chengdu, 610031, China

² School of Urban Railway Transportation, Shanghai University of Engineering Science, Shanghai, 201620, China

³ School of Mechanical Engineering, Southwest Jiaotong University, Chengdu, 610031, China

⁴ Institute of Sound and Vibration Research, University of Southampton, SO17 1BJ, UK

*Correspondence author: shengxiaozhen@hotmail.com

Abstract

In predicting rolling noise from a railway wheelset, some assumptions are usually required to make the calculations less complicated and more efficient. In this study, the effects of some modelling assumptions on the prediction of sound power radiated from a high-speed train wheelset are investigated by using the finite element and boundary element methods. Use is made of the axisymmetry of the wheelset to allow the solution to be obtained in terms of a Fourier series in the circumferential direction. Compared with a moving-wheel formulation, the moving-roughness approach is shown to be sufficient provided that the wheelset receptance takes into account the effects of rotation and the rail receptance accounts for the effect of the moving load. Wheel/rail coupling should take account of lateral as well as vertical forces; neglect of the lateral interaction may result in significant overestimates of the contribution of the axial modes of the wheelset, and thus the overall wheelset radiated noise. If the rotation of the wheelset is not considered, its radiated noise may be underestimated by up to 3 dB at frequencies above 2000 Hz. If the wheelset suspension is not included, the overall sound power would be overestimated at frequencies below 2000 Hz. Compared with symmetric excitation of the wheelset, assuming incoherent excitations for the left and right wheel/rail contacts will significantly affect the radiated noise in the frequency range below 2000 Hz but has negligible effect on the important region above 2000 Hz. Finally, the contribution from the axle is shown to be significant below 1000 Hz. In terms of overall A-weighted level, the effect of the lateral wheel/rail interaction, the rotation of the wheelset and the inclusion of bearings and axleboxes should not be neglected.

Keywords: Sound radiation of wheelset; Wheelset suspension; Rotation of wheelset; Roughness on two rails; Lateral forces; Moving roughness excitation

1. Introduction

In pursuit of green development, many countries are expanding and/or building high-speed railway networks. Although the current maximum operational train speed is already as high as 350 km/h, further increases in speed, up to 400 km/h or even more, are still in many countries' agenda. The main environmental impact of high-speed railways is noise and vibration. A high-speed train generates both aerodynamic and mechanical noise. Although the importance of aerodynamic noise increases at high speed, mechanical rolling noise, through which the wheelset and track radiate noise, also remains important. Past research has shown that the wheelset is the dominant contributor to rolling noise at high frequencies, and becomes increasingly important at high speeds [1]. Prediction of the noise from a wheelset is an important part of rolling noise research.

In order to predict noise from a wheelset, it is necessary to establish a suitable vibration and radiation (i.e. a vibro-acoustic) model. A number of researchers have worked on this topic, but mainly for a single wheel. Remington [2, 3] first proposed an engineering method for predicting wheel/rail rolling noise, in which the wheel was modelled as a rigid mass for predicting wheel vibration, and represented by a series of point sound sources for the evaluation of sound radiation. Schneide et al. [4] simplified the wheel as a disk and used a finite element model (FEM) with ring elements to determine the vibration and the Rayleigh integral equation to calculate sound radiation. Thompson [5, 6] used the axi-harmonic FEM and the boundary element method (BEM) to calculate the vibration and sound radiation of a wheel for different vibration modes defined by the number of nodal diameters. The effects of the number of nodal diameters, wheel radius, and other geometric features were investigated, allowing much more efficient formulae for sound radiation efficiency to be proposed for the wheel. These formulae are implemented in the rolling noise prediction program TWINS, which has been validated by a number of field tests [7, 8]. With advances in computational capability, it has been attempted more recently to use 3D FEM-BEM to predict wheel/rail noise in the time domain [9].

As train operation speeds increase, the effect of wheel rotation receives more and more attention. Thompson [10] first investigated this problem by calculating the response of a wheel to a force rotating around its perimeter. Since the rotation of the wheel is replaced with the rotation of the force, the vibration of the wheel can be calculated using modal summation in which the modes are obtained from an axi-harmonic FE model of the nonrotating wheel. Peaks in the receptance of a rotating wheel occurred at frequencies that are shifted by $\pm n\Omega$ where n is the number of nodal diameters and Ω is the rotational speed. However, this approximation only includes the moving load effect, not the gyroscopic and centrifugal effects caused by wheel rotation. More recently, several studies have been

carried out to predict the vibration of a rotating wheelset more rigorously. Fayos et al. [11] developed a model combining an Eulerian coordinate-based finite element method and modal superposition to obtain the response of spinning solids in the time domain. By coupling the dynamic model of the rotating wheelset with a track model, it was found in Ref. [12] that wheelset rotation has a significant effect on the contact force at frequencies higher than about 1.5 kHz. Baeza et al. [13] presented three models to assess the dynamics of a rotating wheelset: an Eulerian coordinates-based FE model, a modal approach based on Eulerian modal coordinates and an Eulerian coordinates-based axisymmetric model. In Ref. [14], Sheng et al. developed a FE approach based on a 2D mesh for modelling the dynamics of a train wheel in rotation. In this approach, the displacement of the wheel is decomposed into two parts, a rigid body motion part (including the vertical vibration of the wheel axis and the rotation about its axis) and an elastic deformation part. Partial differential equations of motion were established by applying a finite element scheme, which only requires a 2D mesh over the cross-section containing the wheel axis, and the momentum law. The elastic displacement is described in terms of cylindrical coordinates, and is a 2π -periodic function of the circumferential angle about the wheel axis. Thus, the elastic displacement can be expressed as a Fourier series, and the partial differential equations become ordinary differential equations governing the Fourier terms. For a harmonic load rotating (as seen from the wheel) about the wheel axis, these ordinary differential equations can be solved algebraically for steady-state solutions, and the classic Kirchhoff integral equation can be used to evaluate the sound radiation from the rotating wheel [15].

The literature reviewed above shows that the vibro-acoustic models used for a train wheelset have evolved as train speeds have increased and computational capabilities have developed, so that more and more factors can be taken into account. There are many factors which may play a role in rolling noise, in particular for the wheelset which is the focus of the current paper. In addition to its rotation, the wheelset interacts with the track both vertically and laterally (for a train running at a constant speed along a straight track, the longitudinal interaction between the wheelset and track may be neglected), and it also interacts with the superstructure (the axle boxes, primary suspension and bogie frame). The rolling noise model [16] developed recently by the fourth (Sheng), first (Cheng) and fifth (Thompson) authors (it may be termed the SCT model) contains several aspects which are thought to be important for high-speed railways but have been neglected previously. Nevertheless, the lateral interaction between the wheelset and the track and the influence of the superstructure were still excluded.

In this paper, an investigation is conducted into the effects of the various modelling assumptions on the sound power radiated from a high-speed train wheelset. The sound power is calculated using the method proposed in Ref. [15], in which the structural finite element method and the acoustic

boundary element method are applied to the wheelset cross-section for each circumferential order. In Section 2, the vibro-acoustic model for a rotating wheelset is introduced. The effects on the sound power radiated by the wheelset of several factors, of which the values and other parameters values are listed in Section 3, are investigated in Section 4. These include the methods used to obtain the wheel/rail forces, the inclusion of lateral as well as vertical wheel/rail interaction, the influence of the superstructure on the wheelset response, the effect of wheelset rotation, and the assumption of incoherent excitation at the two wheel/rail contacts. The paper is concluded in Section 5.

2. A vibro-acoustic model for a rotating wheelset

In this section, the vibro-acoustic model for a rotating wheelset is briefly introduced. More details can be found in Refs. [14, 15]. The wheelset is assumed to be an axisymmetric elastic body rotating at a constant speed about its main axis.

2.1 The wheelset and its superstructure

The wheelset and the connected bogie frame are shown schematically in Fig. 1. The wheelset is a spinning elastic body and connected to half a bogie frame through the primary suspension and two axle boxes (each with a swivel arm), which are located at the ends of the wheelset axle. The connections between the wheelset and the axle boxes are modelled as springs, which represent the bearings. The primary suspensions consist of two parts in parallel, one of which is a steel spring (usually mounted in series with a rubber element to mitigate the effect of internal resonances) simulated as an undamped spring, and the other is a hydraulic damper that has rubber bushings at the ends which are modelled a spring in series with a viscous damping. As can be seen in Table 2, the mass of the vehicle body is so large and the stiffness of the secondary suspension is so small that the vehicle body only has an effect on the vibration of the wheelset at frequencies of a few hertz, and therefore, they are not included here. The two axle boxes are regarded as rigid bodies vibrating vertically only, and laterally the wheelset is considered to be free. The bogie frame is also simplified to be a rigid body with two degrees of freedom, one being the vertical motion and the other being the roll motion (rotation about the longitudinal axis).

The forces applied to the wheelset (wheel/rail forces and forces applied through the axle boxes) are stationary in space (in a frame of reference moving with the train) but rotate about the wheelset axis if observed from the wheelset, causing moving load effects in the response of the wheelset.

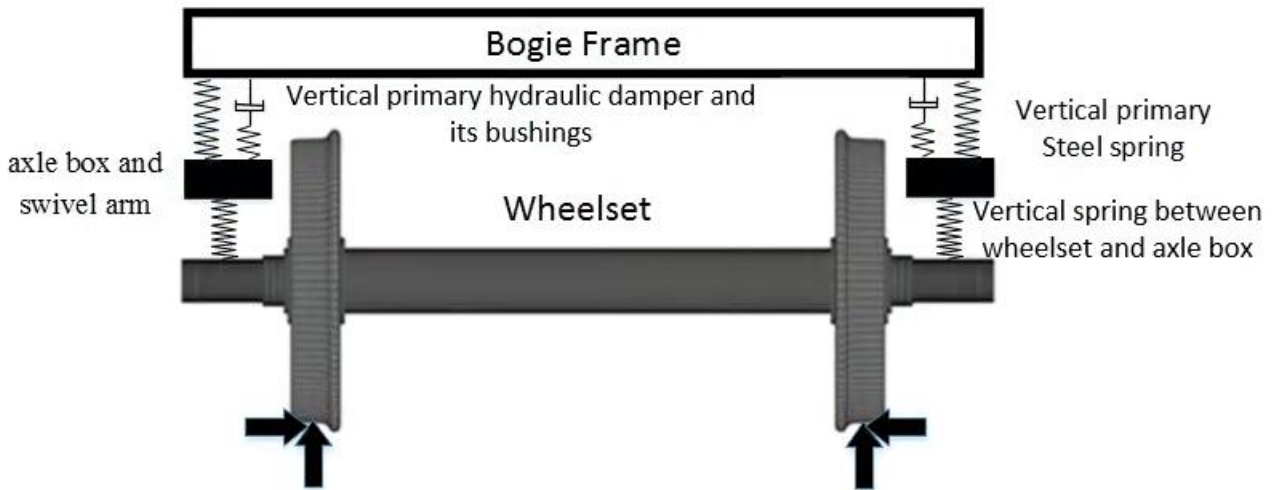


Fig. 1 The wheelset and superstructure. Vertical and lateral wheel/rail forces are indicated.

2.2 Vibration and sound radiation of the wheelset due to stationary harmonic forces

Like many other vibro-acoustic problems, the prediction of sound radiation from the wheelset involves two steps: calculation of in-vacuo vibration of the wheelset, and calculation of sound radiation due to such vibration.

To obtain the vibration of the rotating wheelset, two coordinate systems are required, as shown in Fig. 2. $OXYZ$ is an inertial coordinate system with X in the direction of motion, Z pointing vertically downwards and Y in the lateral direction, and the coordinate origin is at the centroid of the wheelset. The coordinate system $oxyz$ is rigidly attached to the wheelset with the y -axis coinciding with the wheelset axis. At $t = 0$, these two systems coincide with each other. The displacement of the wheelset observed from the $oxyz$ -system is due to its elastic deformation. Thus, the position at an instant t of the deformed wheelset may be obtained by the superposition of two simultaneous motions, a rigid-body motion and an elastic deformation. The rigid-body motion of the wheelset may be decomposed into four components: (1) A translational motion in which the origin o has displacement $u_0(t)$ in the X -direction, $v_0(t)$ in the Y -direction and $w_0(t)$ in the Z -direction; (2) The new coordinate system is rotated by an angle $\alpha(t)$ about the new X -axis (this is the roll angle of the wheelset); (3) It is then rotated by an angle $\beta(t)$ about the new Z -axis (this is the yaw angle of the wheelset), achieving the position of the wheelset axis; (4) Finally the wheelset is rotated by an angle $\Omega_y t$ about its axis (Ω_y is the rotational speed and is assumed to have a value that does not change over time), and the coordinate system becomes $oxyz$, as shown in Fig. 2(a). Note that the direction of this last rotation is opposite to the direction of the y -axis.

As shown in Fig. 2(b), the Cartesian coordinate system $oxyz$ can be transformed into a cylindrical

coordinate system (r, y, θ) , and the displacement associated with the elastic deformation can be decomposed into three components, a radial component (in the r -direction), an axial component (in the y -direction), and a circumferential component (in the θ -direction). The wheelset is cut through its axis to generate a cross-section which is identified by the circumferential angle θ ; a 2D finite element mesh is made on that cross-section (Fig. 3). The boundary, excluding the axis of the cross-section is denoted by Γ . Since the wheelset is axisymmetric, the elastic displacement of a node is a 2π -periodic function of the circumferential angle θ . By applying the momentum law and the momentum torque law, and following the standard procedure of the finite element method, differential equations of motion can be established for the wheelset to govern the rigid body motions and the elastic displacement. It is shown in Ref. [14] that, by decomposing the elastic displacement into components at particular circumferential orders (denoted by m), these components, as well as the rigid body motions, can be determined algebraically for harmonic forces that are stationary in space. The circumferential order m can be either positive or negative, while its absolute value represents the number of nodal diameters (n).

It is shown in Ref. [14] that the rigid body motions defined above and the displacements of the loading points are all harmonic at the same frequency as the excitation frequency. Thus, a receptance can be readily defined for a wheel/rail contact point. Furthermore, if a sliding condition is assumed between the wheelset surface and the surrounding air, air particles in contact with the wheelset will also vibrate harmonically at the same frequency as the excitation frequency. The vibrational velocity of an air particle at instant t is equal to the normal (to the wheelset surface) velocity of a point on the wheelset surface which is just passing the air particle at that instant. It is denoted by $v_j(\theta, t)$ if the air particle is associated with the j -th node. Thus, it can be written as

$$v_j(\theta, t) = \hat{v}_j(\theta)e^{i\Omega t} . \quad (1)$$

Since $\hat{v}_j(\theta)$ is 2π -periodic function of the circumferential angle θ , it can be expressed as

$$\hat{v}_j(\theta) = \sum_{m=-\infty}^{\infty} \bar{v}_{jm} e^{im\theta} . \quad (2)$$

The air particle velocity, $v(r, y, \theta, t)$, at any other point on the surface defined by (r, y, θ) can be interpolated from the nodal velocities.

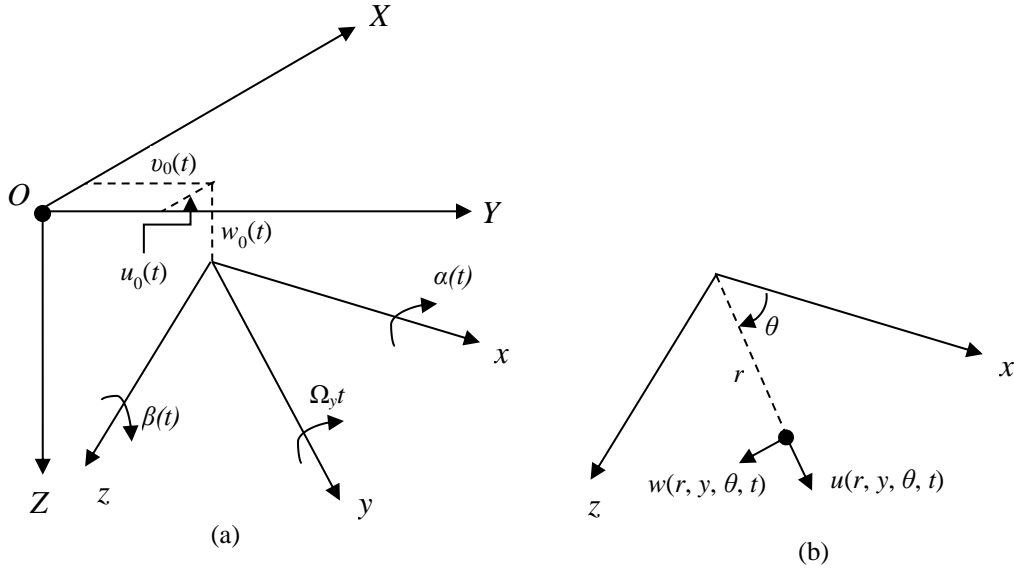


Fig. 2 Rigid-body motions and elastic displacements. (a) Rigid-body motion components; (b) elastic displacement components.

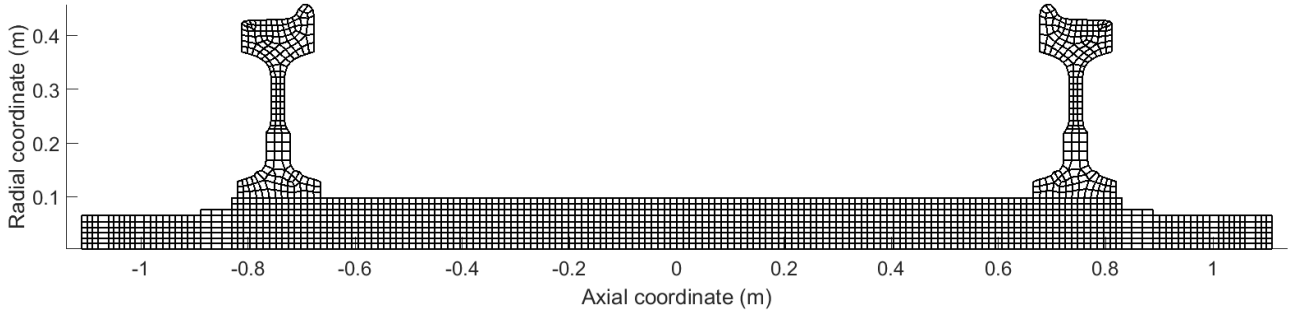


Fig. 3 A two-dimensional finite element mesh on the cross-section of the wheelset.

Air particle velocities given in Eqs. (1) and (2) generate harmonic sound waves propagating in the air surrounding the wheelset and these sound waves can be predicted using the conventional acoustic boundary element method. Since now the boundary of the acoustic domain is axisymmetric, the axisymmetric boundary element method can be applied to obtain the sound pressure for each circumferential order \bar{p}_m [15]. The sound power radiated from the surface of the wheelset can be obtained as [15]:

$$W_w = \pi \sum_{m=-\infty}^{\infty} \int_{\Gamma} \left(\text{Re}[\bar{p}_m(r, y)] \text{Re}[\bar{v}_m(r, y)] + \text{Im}[\bar{p}_m(r, y)] \text{Im}[\bar{v}_m(r, y)] \right) r d\Gamma \quad (3)$$

where Γ is the acoustic boundary, \bar{p}_m is the amplitude of the sound pressure component at the m th circumferential order, \bar{v}_m is the amplitude of the normal velocity of the boundary at the m th circumferential order, r and y are the radial and axial coordinates of the integration point on Γ .

By using Eq. (3), sound power radiated by the rotating wheelset can be obtained. However, the

effect of wheelset speed on the sound power has not been considered at the moment. This involves predictions of sounds radiated by a moving and vibrating object. Although a boundary integral equation has been derived in In Ref. [17] for sound radiation from a moving and vibrating object, its numerical solution is still yet to be progressed.

2.3 Wheel/rail forces

In Section 2.2, the forces applied to the wheelset are stationary harmonic forces at a single frequency (the excitation frequency). In reality, the most important dynamic forces applied to the wheelset are the wheel/rail forces, which are to be determined. The wheel/rail forces are determined by considering interactions between the wheelset and the track, both having certain roughness on the rolling surfaces. Both the vertical and lateral wheel/rail interactions may be considered. Previously, the moving-roughness approach has commonly been used to determine the wheel/rail forces [1]. According to this approach, if the wheel/rail forces at the left and right wheels are subject to the same roughness, these forces are given by

$$\mathbf{P}(\omega) = -[\mathbf{D}_w(\omega) + \mathbf{D}_R(\omega) + \mathbf{D}_C(\omega)]^{-1} \mathbf{Z}(\omega), \quad (4)$$

where,

$$\begin{aligned} \mathbf{D}^w(\omega) &= \begin{bmatrix} d_{VV}^w(\omega) & d_{VH}^w(\omega) \\ d_{HV}^w(\omega) & d_{HH}^w(\omega) \end{bmatrix}, & \mathbf{D}^R(\omega) &= \begin{bmatrix} d_{VV}^R(\omega) & 0 \\ 0 & d_{HH}^R(\omega) \end{bmatrix} \\ \mathbf{D}^C(\omega) &= \begin{bmatrix} d_V^C(\omega) & 0 \\ 0 & d_H^C(\omega) \end{bmatrix}, & \mathbf{Z}(\omega) &= \begin{bmatrix} z(\omega) \\ 0 \end{bmatrix}, & \mathbf{P}(\omega) &= \begin{bmatrix} P_V(\omega) \\ P_H(\omega) \end{bmatrix} \end{aligned} \quad (5)$$

where d^w , d^R and d^C are the receptances of the wheel, rail and contact spring at the wheel/rail contact point; subscripts V and H represent, respectively, the vertical and lateral directions, e.g., d_{VV}^w stands for the vertical displacement of the wheel at the wheel/rail contact point due to a unit vertical wheel/rail force; $z(\omega)$ is the vertical wheel/rail roughness; $P_V(\omega)$ and $P_H(\omega)$ are the vertical and lateral wheel/rail forces. For the wheelset, these receptances assume symmetry at the centre of the axle and are therefore the response to a unit force acting on both wheels. As already stated, Ref. [14] presents a method for calculating the required receptances for the wheel. For the rail, the receptances in the vertical and lateral directions are calculated using the methods presented in Refs. [18, 19]. For the vertical direction the rail is represented by a periodically supported Timoshenko beam whereas in the lateral direction a multiple beam approach is used to include the effects of rail cross-section deformation. It can be seen in Eq. (5) that, the cross receptance of the rail between the vertical and lateral directions is neglected; it is generally small when the contact point is near the centreline of the

rail [1].

The moving-roughness approach cannot take into account the parametric excitation mechanism due to the periodic nature of the track. To overcome this problem, a moving-wheel approach should be applied. In this paper, wheel/rail forces are calculated using the moving-wheel method described in Ref. [20]. According to this method, the combined wheel/rail roughness experienced by the wheelset is assumed to be periodic in the track direction, with the period being a multiple (denoted by N) of the track period (e.g. the fastener spacing or, for a slab track with discrete slabs, the slab length). The steady-state wheel/rail force $\mathbf{P}(\omega)$ can be obtained by solving a set of algebraic equations. The wheel/rail force is determined at a frequency resolution of the track period-passing frequency divided by N .

2.4 Sound power radiated by a wheelset subject to symmetric wheel/rail forces

If the left wheel/rail roughness is identical to the right wheel/rail roughness, then the wheel/rail forces are symmetric. The spectrum of the sound power radiated by a wheelset due to the symmetrical wheel/rail forces is given by:

$$W(\omega) = \pi \sum_{m=-\infty}^{\infty} \int_{\Gamma} \left(\begin{aligned} &\text{Re}[P_V(\omega)\bar{p}_{V_m}(r, y, \omega) + P_L(\omega)\bar{p}_{H_m}(r, y, \omega)] \text{Re}[P_V(\omega)\bar{v}_{V_m}(r, y, \omega) + P_H(\omega)\bar{v}_{H_m}(r, y, \omega)] \\ &+ \text{Im}[P_V(\omega)\bar{p}_{V_m}(r, y, \omega) + P_L(\omega)\bar{p}_{H_m}(r, y, \omega)] \text{Im}[P_V(\omega)\bar{v}_{V_m}(r, y, \omega) + P_H(\omega)\bar{v}_{H_m}(r, y, \omega)] \end{aligned} \right) r d\Gamma \quad (6)$$

where $P_V(\omega)$ and $P_H(\omega)$ are the vertical and lateral wheel/rail forces predicted in Section 2.3; \bar{p}_{V_m} and \bar{v}_{V_m} are the sound pressure on, and normal velocity of, the wheelset surface at the m th circumferential order due to a unit vertical wheel/rail force applied at each wheel/rail contact point; similarly \bar{p}_{H_m} and \bar{v}_{H_m} are the sound pressure on, and normal velocity of, the wheelset surface at the m -th circumferential order due to a unit lateral wheel/rail force applied at each wheel/rail contact point. The sum over the circumferential orders must be truncated. It is found that $|m| \leq 7$ is sufficient for a train wheelset running at 350 km/h and for frequencies up to 5000 Hz. The surface integral is taken over the boundary Γ of the wheelset including both wheels and the axle.

If only the vertical wheel/rail interaction is taken into account, Eq. (6) becomes

$$\begin{aligned} W(\omega) &= \pi \sum_{m=-\infty}^{\infty} \int_{\Gamma} \left(\begin{aligned} &\text{Re}[P_{VV}(\omega)\bar{p}_{V_m}(r, y, \omega)] \text{Re}[P_{VV}(\omega)\bar{v}_{V_m}(r, y, \omega)] \\ &+ \text{Im}[P_{VV}(\omega)\bar{p}_{V_m}(r, y, \omega)] \text{Im}[P_{VV}(\omega)\bar{v}_{V_m}(r, y, \omega)] \end{aligned} \right) r d\Gamma \\ &= |P_{VV}(\omega)|^2 \pi \sum_{m=-\infty}^{\infty} \int_{\Gamma} \left(\begin{aligned} &\text{Re}[\bar{p}_{V_m}(r, y, \omega)] \text{Re}[\bar{v}_{V_m}(r, y, \omega)] \\ &+ \text{Im}[\bar{p}_{V_m}(r, y, \omega)] \text{Im}[\bar{v}_{V_m}(r, y, \omega)] \end{aligned} \right) r d\Gamma \\ &= |P_{VV}(\omega)|^2 W_{wV}(\omega) \end{aligned} \quad (7)$$

where $P_{VV}(\omega)$, which is in general different from $P_V(\omega)$ in Eq. (6), is the vertical wheel/rail force due to vertical wheel/rail interaction only and the term $W_{wr}(\omega)$ is the sound power due to a unit vertical force acting on both wheels.

2.5 Sound power radiated by a wheelset subject to incoherent excitation at the two wheel/rail contacts

In Section 2.4, the left and right wheel/rail roughness spectra have been assumed to be identical, not only in magnitude but also in phase. This is normally not the case in reality. In fact, according to [27], for rolling noise prediction, the right and left wheel/rail roughness can be regarded as incoherent.

Considering a case in which the magnitudes of the left and right wheel/rail roughness are equal but the phase difference is Ψ , Eq.(4) and Eq.(5) can be extended to be :

$$\mathbf{P}(\omega) = -[\mathbf{D}^W(\omega) + \mathbf{D}^R(\omega) + \mathbf{D}^C(\omega)]^{-1} \mathbf{Z}(\omega), \quad (8)$$

$$\mathbf{D}^W(\omega) = \begin{bmatrix} d_{VL,VL}^W(\omega) & d_{VL,HL}^W(\omega) & d_{VL,VR}^W(\omega) & d_{VL,HR}^W(\omega) \\ d_{HL,VL}^W(\omega) & d_{HL,HL}^W(\omega) & d_{HL,VR}^W(\omega) & d_{HL,HR}^W(\omega) \\ d_{VR,VL}^W(\omega) & d_{VR,HL}^W(\omega) & d_{VR,VR}^W(\omega) & d_{VR,HR}^W(\omega) \\ d_{HR,VL}^W(\omega) & d_{HR,HL}^W(\omega) & d_{HR,VR}^W(\omega) & d_{HR,HR}^W(\omega) \end{bmatrix}, \mathbf{D}^R(\omega) = \begin{bmatrix} d_{V,V}^R(\omega) & 0 & 0 & 0 \\ 0 & d_{L,L}^R(\omega) & 0 & 0 \\ 0 & 0 & d_{V,V}^R(\omega) & 0 \\ 0 & 0 & 0 & d_{L,L}^R(\omega) \end{bmatrix} \quad (9)$$

$$\mathbf{D}^C(\omega) = \begin{bmatrix} d_V^C(\omega) & 0 & 0 & 0 \\ 0 & d_L^C(\omega) & 0 & 0 \\ 0 & 0 & d_V^C(\omega) & 0 \\ 0 & 0 & 0 & d_L^C(\omega) \end{bmatrix}, \mathbf{Z}(\omega) = \begin{bmatrix} z(\omega) \\ 0 \\ z(\omega)e^{-i\Psi} \\ 0 \end{bmatrix}, \mathbf{P}(\omega) = \begin{bmatrix} P_{VL}(\omega) \\ P_{HL}(\omega) \\ P_{VR}(\omega) \\ P_{HR}(\omega) \end{bmatrix},$$

where, for example, $d_{HL,VR}^W(\omega)$ is the lateral displacement at the wheel/rail contact point of the left wheel due to a vertical unit wheel/rail force on the right wheel. This naming convention applies to other variables in $\mathbf{D}^W(\omega)$ as well.

If the left and right roughnesses are independent of each other, the radiated sound power can be calculated by

$$W(\omega) = W_L(\omega) + W_R(\omega), \quad (10)$$

where W_L and W_R are the sound power radiated by wheelset when excited by roughness $\mathbf{Z}_1(\omega) = [z(\omega) \ 0 \ 0 \ 0]^T$ and $\mathbf{Z}_2(\omega) = [0 \ 0 \ z(\omega) \ 0]^T$, respectively. These can be obtained from combinations of the response to symmetric and anti-symmetric excitation.

3 Parameters used in this paper

Results will be presented and discussed in Section 4 and this section is just to describe the parameters of the bogie frame, primary suspension, wheelset and track, which are used to produce

the results. The density of air is 1.21 kg/m^3 and the sound speed is 344 m/s .

3.1 Parameters of the wheelset and the superstructure

The material parameters of the wheelset are listed in Table 1 and the parameters of the superstructure are listed in Table 2. Rubber bushings are installed on both sides of a hydraulic damper, and the stiffness value in Table 2 is the resultant stiffness of the two in-series bushings. The mass of the hydraulic damper and the metal suspension spring are neglected. The stiffness between the axle and axle box in Table 2 is an estimate obtained from the contact cross-sectional area of the bearings, and in the absence of measured data the loss factor is taken as 0.1.

Table 1 Parameters of the wheelset

Density	Young's modulus	Poisson's ratio	Loss factor	Mass	Radius
7850 kg/m^3	$2.1 \times 10^{11} \text{ N/m}^2$	0.3	0.0002	1105.3 kg	0.43 m

Table 2 Parameters of the superstructure

Mass of a quarter of the vehicle body	9000 kg
Stiffness of half a secondary suspension	$4 \times 10^5 \text{ N/m}$
Mass of axle box and rotary arm	203 kg
Mass of half bogie frame	1300 kg
The moment of inertia in roll of half bogie frame	$900 \text{ kg} \cdot \text{m}^2$
Stiffness between axle and axle box	$5 \times 10^9 \text{ N/m}$
Loss factor between axle and axle box	0.1
Primary vertical stiffness of steel spring	$2.08 \times 10^6 \text{ N/m}$
Primary vertical damping coefficient of hydraulic damper	$1 \times 10^4 \text{ N} \cdot \text{s/m}$
Stiffness of the rubber bushings	$5 \times 10^6 \text{ N/m}$
Loss factor of the rubber bushings	0.1
Transverse distance between two primary suspensions	2 m

3.2 Parameters of the track

The parameters of the track are listed in Table 3 for vertical dynamics and Table 4 for lateral dynamics. In the track model, the track slab may be considered to be rigid or flexible. These two treatments are compared in Fig. 4 in terms of the vertical rail receptance. As can be seen in Fig. 4, the difference is negligible, so in this paper the track slab is regarded as rigid to simplify the calculations.

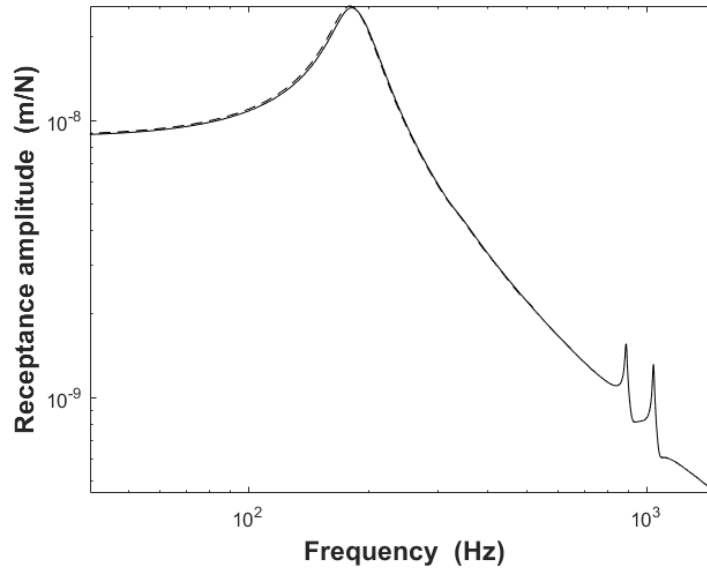


Fig. 4 Vertical driving point receptance of the rail at mid-span for a load moving at 350 km/h. —, rigid track slab; ---, flexible track slab.

The vertical and lateral driving point receptances of the rail at mid-span are shown in Fig. 5 for a load moving at 350 km/h. It can be seen from Fig. 5 that for a vertical force, the rail-on-pad resonance frequency is about 184 Hz, and the pinned-pinned frequency is split into two, with peaks at 887 Hz and 1041 Hz. For a lateral force, the rail-on-pad resonance frequency is around 68 Hz while the pinned-pinned frequency is shifted downwards to 349 Hz and upwards to 503 Hz. It can be checked that $350/3.6/(1041-887) = 350/3.6/(503-349) = 0.631$ m, slightly different from the sleeper space 0.64 m. This may be explained by the fact that the track model considers the width of the fastener in the track direction, allowing the fastener to provide a moment to the rail.

Table 3 Parameters used for vertical dynamics of the track [21]

Density of the rail	7850 kg/m ³
Young's modulus of the rail	2.1×10^{11} N/m ²
Shear modulus of the rail	0.81×10^{11} N/m ²
Cross-sectional area of the rail	7.69×10^{-3} m ²
Second moment of area of the rail	30.55×10^{-6} m ⁴
Shear coefficient of the rail cross-section	0.4
Vertical rail pad stiffness	5.44×10^7 N/m
Rail pad loss factor	0.25
Fastener spacing	0.64 m
Support width of fastener in track direction	0.25 m
Length, width and thickness of track slab	6.35 m, 2.8 m, 0.28 m
Vertical stiffness of the concrete-asphalt layer under slab	6.67×10^9 N/m ²

Loss factor of the concrete–asphalt layer under slab	0.1
--	-----

Table 4 Parameters used for lateral dynamics of the track [18]

Height of the rail head	0.039 m
Width of the rail head	0.073 m
Shear coefficient of the rail head	0.85
Second moment of area of the rail head	$1.264 \times 10^{-6} \text{ m}^4$
Polar second moment of area of the rail head	$1.625 \times 10^{-6} \text{ m}^4$
Equivalent polar second moment of area of the rail head	$0.9549 \times 10^{-6} \text{ m}^4$
Height of the rail foot	0.0175 m
Width of the rail foot	0.15 m
Shear coefficient of the rail foot	0.85
Second moment of area of the rail foot	$4.921 \times 10^{-6} \text{ m}^4$
Polar second moment of area of the rail foot	$4.988 \times 10^{-6} \text{ m}^4$
Equivalent polar second moment of area of the rail foot	$0.2471 \times 10^{-6} \text{ m}^4$
Height of the rail web	0.114 m
Width of the rail web	0.019 m
Second moment of area of the rail web	$0.5716 \times 10^{-6} \text{ m}^4$
Lateral railpad stiffness	$150 \times 10^6 \text{ N/m}$
Rotational stiffness	$1.02 \times 10^5 \text{ N m/rad}$

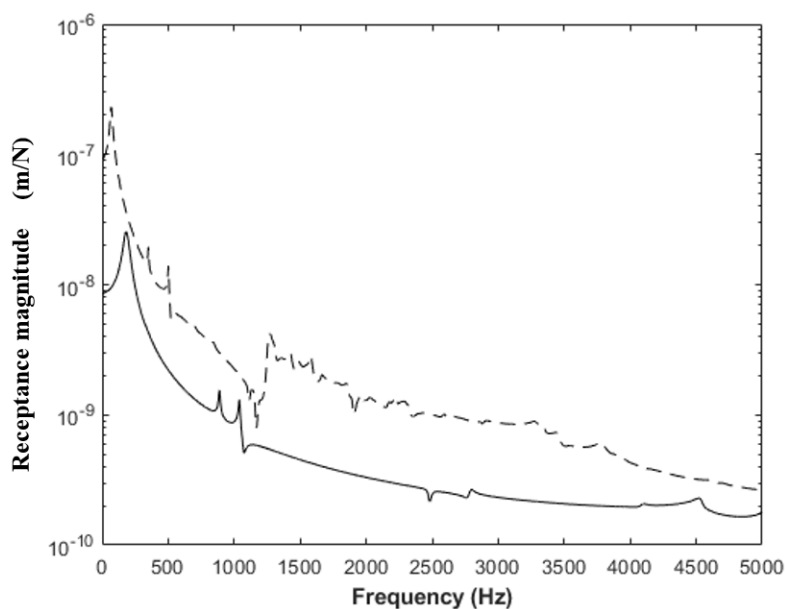


Fig. 5 Driving point receptance of the rail at mid-span for a load moving at 350 km/h. —, vertical; ---, lateral.

3.3 Axle load and wheel/rail contact stiffness

Half of the axle load is 78.4 kN, and the vertical stiffness of the linearised Hertz contact spring

is estimated to be 1.31×10^9 N/m. Based on Ref. [22], a loss factor of $3.3 \times 10^{-6} f$ is given to the contact spring to account for energy loss in the bodies in contact, where f is the frequency. According to Ref. [1], the lateral contact may be simulated by a spring and a viscous damper in series, with the damper representing the lateral creep force. Based on the wheel/rail parameters, the stiffness of the spring is estimated to be 9.71×10^8 N/m and the damping coefficient of the damper is 1.56×10^5 N s/m.

3.4 Wheel/rail roughness

The roughness spectrum used (in solid line) in this paper and a wheel/rail roughness (in dashed line and contact patch-filtered) measured in a Chinese high-speed railway line are shown in narrow band form in Fig. 6. The solid line is synthesised from the upper limit curve for the acoustic rail roughness (ISO 3095: 2013) [23] in the short wavelength range (< 0.71 m) and the low disturbance ORE (ERRI) spectrum [24] in the long wavelength range (> 2 m). The spectrum is obtained in this way initially in terms of 1/3 octave wavelength bands. To predict wheel/rail forces, the roughness spectrum must be converted into a narrow-band spectrum (Fig. 6). To account for the stochastic nature of the roughness, a random phase angle, which is assumed to be uniformly distributed over $[0, 2\pi]$, is generated independently for each wavenumber component of the wheel/rail narrow-band roughness spectrum.

It is well known that wheel/rail contact patch has a filtering effect for the roughness. The actual roughness level in dB should be attenuated by a filter characteristic, $L_z(\lambda)$, which is a function of the roughness wavelength. An approximation for $L_z(\lambda)$ is given in Ref. [1] as,

$$L_z(\lambda) = 20 \log_{10}(1 + 0.25\pi(2\pi a / \lambda)^3), \quad (11)$$

where a is half the length of the contact patch in the running direction and λ is roughness wavelength. For the wheel, rail and axle load considered here, a is estimated to be 6.59 mm. The narrow-band roughness spectrum after considering the filtering effect is shown in dash-dotted line in Fig. 6.

The dashed line in Fig. 6 is taken from Ref. [16] with magnitude adjusted to account for difference in wavenumber resolution between Fig. 6 and Ref. [16]. The roughness spectrum in Ref. [16] with wavelengths less than 0.5 m were generated from field measurement on a slab track line and wheels. From Fig. 6 it can be seen that, the measured roughness is higher than the roughness used, but the rate of change with wavelength is approximately the same for both.

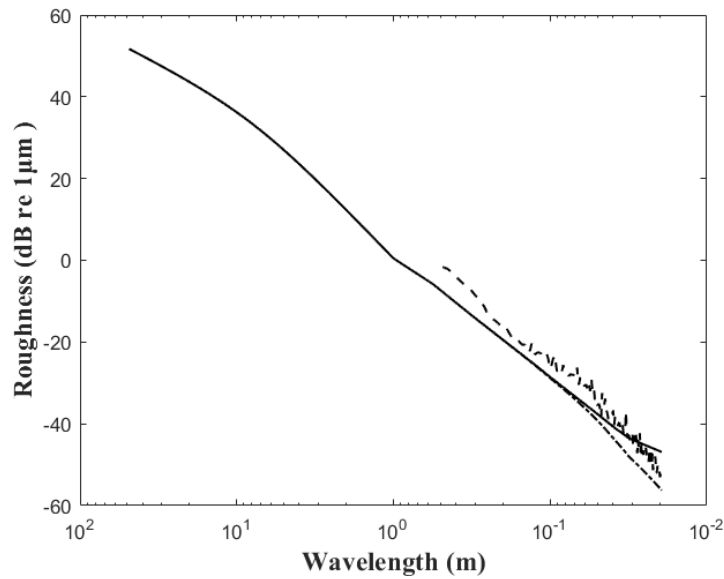


Fig. 6 The narrow band wheel/rail roughness spectrum in dB re 1 μm at a wavenumber resolution of 0.0065 rad/m (at a speed of 350 km/h, the excitation frequency resolution is 0.1 Hz). —, original; - • -, contact patch-filtered; - - -, measured wheel/rail roughness (contact patch-filtered) [16].

3.5 Frequency resolution

For a wheelset without any damping treatment, the loss factor is very low and the frequency resolution of any spectrum must be sufficiently high, otherwise some resonances may not be accurately caught by the spectrum [1]. In the calculations presented in Section 4, the vibration and sound radiation of the wheelset due to unit harmonic wheel/rail forces are first calculated at a frequency spacing of 2 Hz, producing a frequency spectrum which can approximately show the resonance frequencies. Around each approximate resonance frequency, the vibration and sound radiation of the wheelset are recalculated at a finer frequency resolution of 0.1 Hz. The spectrum at other frequencies are refined to the higher frequency resolution using interpolation. As a result, a spectrum at a frequency resolution of 0.1 Hz is produced. This frequency resolution is sufficient since, according to previous research [1], it is normally above about 1500 Hz that the wheelset becomes the main radiator for rolling noise; at this frequency, the half power bandwidth of wheel resonances is at least 0.3 Hz, three times the frequency resolution.

4. Effects of modelling assumptions on wheelset-radiated sound power

As discussed above, the wheelset is in rotation and interacts with the track both vertically and laterally, as well as with its superstructure (the axle boxes, primary suspension and bogie frame). Consideration of all those factors together is often considered to make the predictions of wheel/rail forces and rolling noise too complicated, and it may be necessary to introduce some modelling

assumptions. Various modelling assumptions may be applied, such as replacement of the motion of the wheelset with the moving-roughness approach, neglect of lateral wheelset/track interaction, exclusion of the superstructure, use of a non-rotating wheelset instead of a rotating one, etc. In this section, the effects of these modelling assumptions on the wheel/rail forces and wheelset-radiated sound power due to wheel/rail roughness are studied. The case in which all the factors mentioned above are included is taken to be a benchmark, based on which the effects of the various approximations are assessed. Unless otherwise stated, symmetric wheel/rail roughness (i.e. both wheels experience the same wheel/rail roughness) is assumed and the rotation speed of the wheelset Ω_y is about 226 rad/s (or 36 Hz), corresponding to a train speed of 350 km/h.

4.1 Comparison of moving-roughness method and moving-wheel method

In Section 2.3, two methods of calculating wheel/rail force in the frequency domain are introduced, the moving-roughness method and the moving-wheel method. Although the second one, which allows the wheelset to roll and move at high speed along the track, is used for most of the cases in this paper, it incurs a much higher computational cost and a comparison between these two methods is worthwhile. Results are shown in Fig. 7 in terms of the wheel/rail forces. For the moving-roughness method, different choices can be made for the receptance for the rail and wheel: for the wheel, the receptance can be that of the wheel in rotation or not; for the rail, the receptance can be for a moving force or a stationary force. The wheel/rail force shown in Fig. 7 for the moving-roughness method is based on the receptance of the rotating wheel and the receptance of the rail for a moving force at mid-span.

From Fig. 7(a) it can be seen that the two methods produce almost the same result for most frequencies. However, significant differences do exist between these two methods at two sets of frequencies, one being the sleeper-passing frequency (152 Hz) and its multiples, and the other being those around the pinned-pinned frequency of the rail. The moving-roughness method, due to its nature, cannot predict wheel/rail force components due to parametric excitation at the sleeper-passing frequency and its multiples. Moreover, since the dynamic properties of the rail seen by the wheel change significantly from mid-span to fastener positions [18], use of only the dynamics at mid-span in the moving-roughness method results in a less fluctuating wheel/rail force around the pinned-pinned frequency. These observations can be equally applied to the lateral force shown in Fig. 7(b).

From Fig. 7(a)(b) it can be seen that the lateral force is much smaller than the vertical force. The ratio of the vertical force to the lateral force is shown in Fig. 7(c). In both wheel/rail force calculation methods, the vertical and lateral wheel/rail forces are proportional to the vertical wheel/rail roughness (see Eqs. (4) and (5)); therefore, the vertical-lateral force ratio will not change with the wheel/rail

roughness.

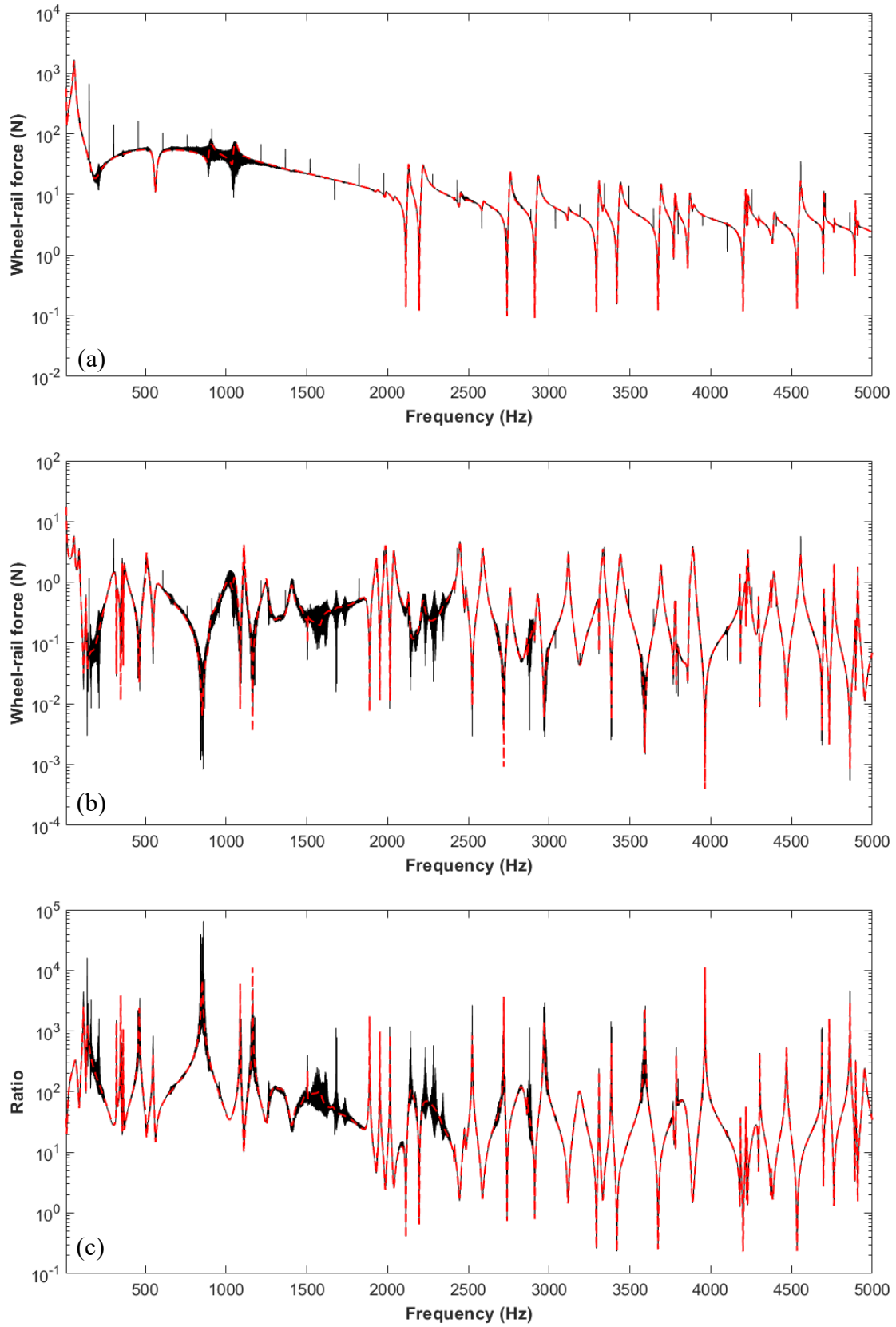


Fig. 7 The wheel/rail force at 350 km/h. (a) Vertical; (b) Lateral; (c) Vertical-to-lateral ratio; —, the moving-wheel method; ---, the moving roughness method.

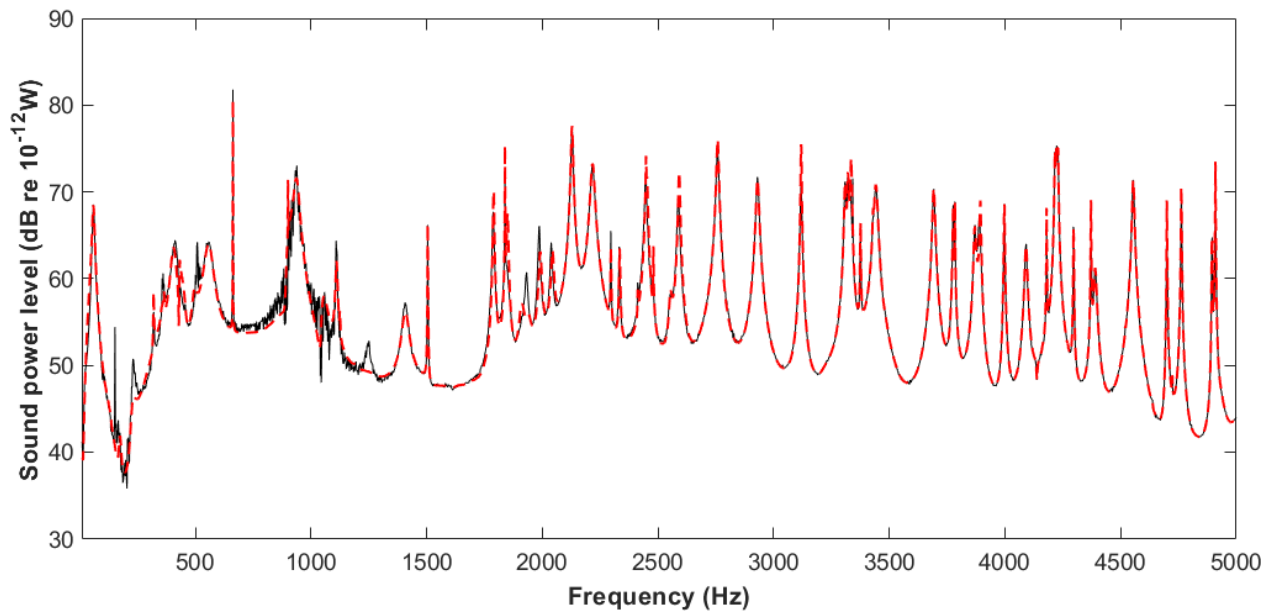


Fig. 8 Sound power level from the wheelset in narrow bands at 350 km/h. —, the moving-wheel method; - -
 —, the moving roughness method.

Although the lateral wheel/rail force is relatively small at most frequencies, there are some frequencies where the lateral force is greater, and it is still worthwhile checking its effect on the vertical wheel/rail force, as discussed in Section 4.2 below.

The sound power radiated by the wheelset is determined using the forces obtained by these two methods. Fig. 8 compares these results, and shows that the sound power spectra obtained by the two methods are almost identical, apart from some differences around the pinned-pinned frequency. The peaks at the sleeper-passing frequency and its multiples do not appear in the sound power spectrum. However, the difference between these two methods for the track radiation is likely to be more significant and needs further investigation.

4.2 Effect of including lateral wheel/rail interaction

Fig. 9 compares the vertical wheel/rail force obtained with and without including the lateral interaction. In the latter case, the wheelset is assumed to be subject to forces at the wheel/rail contact points in the vertical direction only, and the predicted vertical wheel/rail force, compared with the former case, has sharper dips at frequencies (indicated by arrows) associated with axial wheel modes (modified by wheelset rotation). At these frequencies, the lateral wheel/rail force shown in Fig. 7(b) exhibits peaks. When the lateral wheel/rail interaction is taken into account, these dips are substantially suppressed.

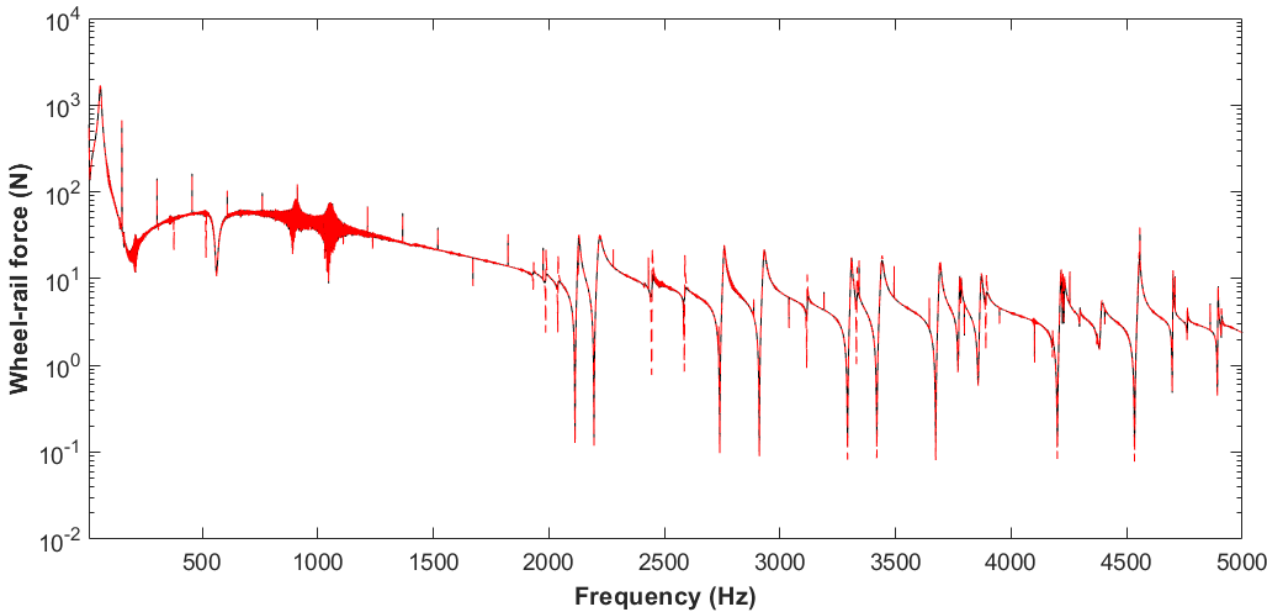


Fig. 9 The vertical wheel/rail force predicted using the moving-wheel method. —, with lateral wheel/rail interaction; ---, without lateral wheel/rail interaction.

The sound power from the rotating wheelset may be predicted by considering both the vertical and lateral wheel/rail interactions (Eq. (6)), or just by considering the vertical wheel/rail interaction (Eq. (7)). The results are shown in Fig. 10. Various peaks occur in the figure that correspond to wheel/rail force peaks in Fig. 9. There are differences in sound power between these two predictions at some frequencies above about 300 Hz. The main feature of the differences is that the peaks are much higher if the lateral wheel/rail interaction is neglected. In other words, significant damping is introduced to the wheelset by the lateral wheel/rail interaction. By comparing Fig. 9 and Fig. 10, it can be seen that the differences occur mainly at the frequencies where the lateral interaction has a strong effect on the vertical wheel/rail forces.

Some of these peaks in the dashed curve (without lateral wheel/rail interaction) are identified in pairs by a pair of numbers (n, p) . The two frequencies of the pair with numbers (n, p) are the result of frequency splitting from the natural frequency of the non-rotating wheelset at nodal diameter number n and nodal circle number p . The splitting is caused by wheelset rotation. These modes (shown in Fig. 11) are axial modes of the non-rotating wheelset which will be damped by the lateral wheel/rail interaction.

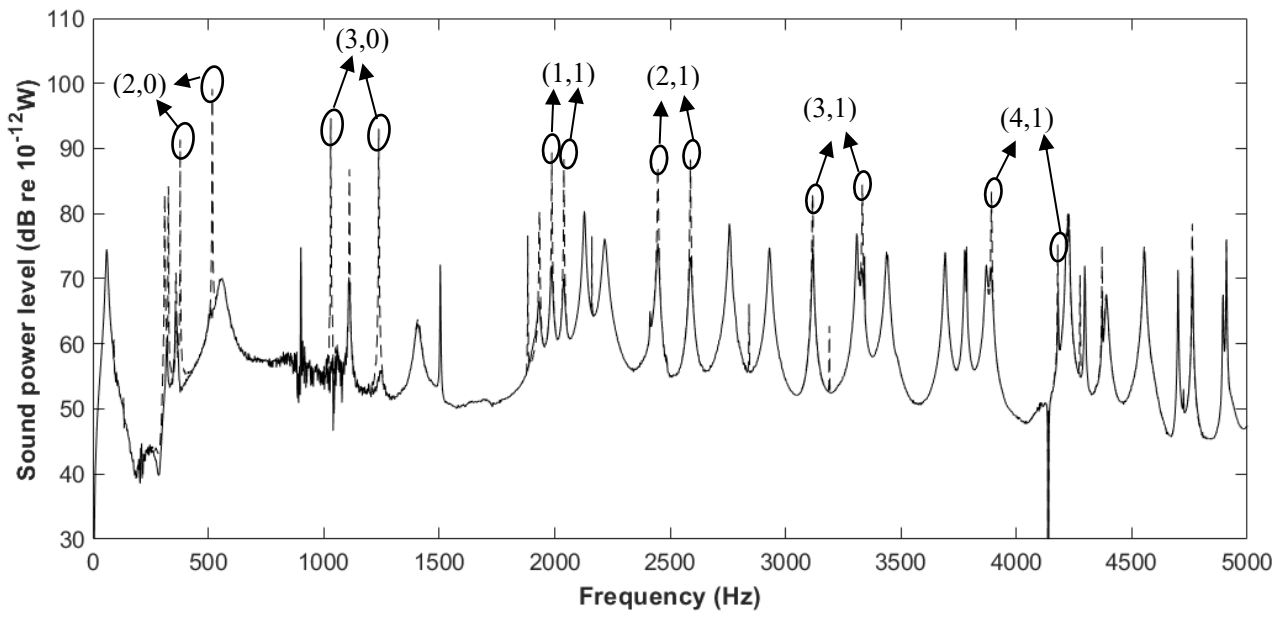


Fig. 10 Sound power from the wheelset. —, predicted with both the vertical and lateral wheel/rail interactions; -----, predicted with vertical wheel/rail interaction only.

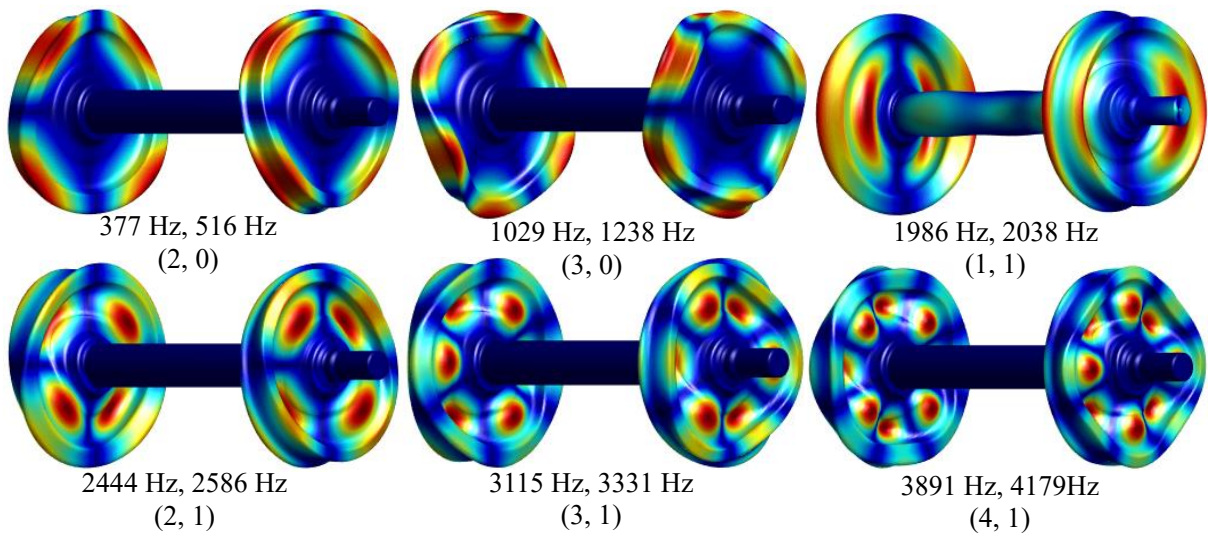


Fig. 11 Vibration modes of the wheelset suppressed due to lateral wheel/rail interaction

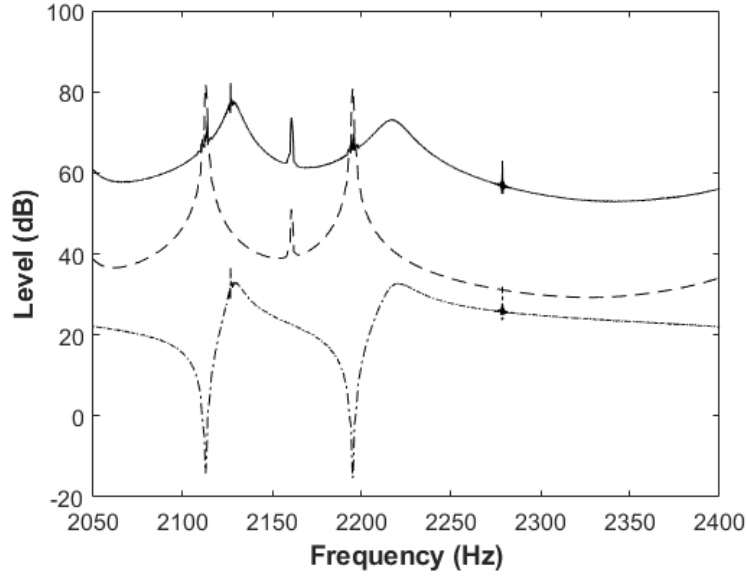


Fig. 12 The three levels defined in Eq. (12). —, the actual sound power level; ---, the sound power level for a unit vertical force; - • -, the vertical wheel/rail force level.

Other peaks in the sound power are mainly associated with radial modes. At these peaks, the two predictions are similar to each other. At these frequencies, the radial modes dominate the sound radiation and the lateral wheel/rail interaction plays a less important role. Thus, sound power of the wheelset can be calculated using Eq. (7), i.e. in decibels,

$$L_w(\omega) \approx 10\log_{10}\left(\left(|P_{VV}(\omega)|^2 W_{wv}/1 \times 10^{-12}\right)\right) = 10\log_{10}\left(|P_{VV}(\omega)|^2\right) + 10\log_{10}\left(W_{wv}/1 \times 10^{-12}\right) \quad (12)$$

The first term on the right-hand side is termed the wheel/rail force level and the second one is the sound power level for two unit vertical forces, applied at the right and left wheel/rail contact points. The three terms in Eq. (12) are shown in Fig. 12 over a frequency range from 1800 Hz to 2400 Hz, including a mode (2, r) in which the wheel/rail force depends more on the dynamics of the wheelset than the track. It can be seen that at the two resonance frequencies of the rotating wheelset (which are split from a single modal frequency of the nonrotating wheelset by wheelset rotation), the unit force sound power level has sharp peaks while the wheel/rail force level exhibits sharp dips. The sharpness is due to the low material damping of the wheelset. However, the actual sound power level radiated by the wheelset, which, according to Eq. (12), is the sum of the wheel/rail force level and the unit force sound power level, contains two broad peaks at frequencies above the corresponding wheelset frequencies [1]. Adding damping to the wheelset will reduce the sharpness of the peaks and dips mentioned above, but probably not have a significant effect on the sound power level of the wheelset, unless the added damping is sufficiently high [1].

4.3 Effect of wheelset rotation

The wheelset receptance, wheel/rail force and sound power may be calculated with or without considering wheelset rotation. The effect of wheelset rotation on the predicted wheel/rail force has recently been extensively discussed in Ref. [26] using a time-domain approach. In Ref. [26], for particular wheel/rail roughness wavelengths, the predicted wheel/rail force can be significantly different if wheelset rotation is not taken into account. This section uses the moving-wheel approach to further study the effect of wheelset rotation on the sound power of the wheelset. Both vertical and lateral interaction are included.

Sound power levels of the wheelset predicted with and without consideration of wheel rotation are compared in Fig. 13 in terms of narrow bands and in Fig. 14 in terms of 1/3 octave bands.

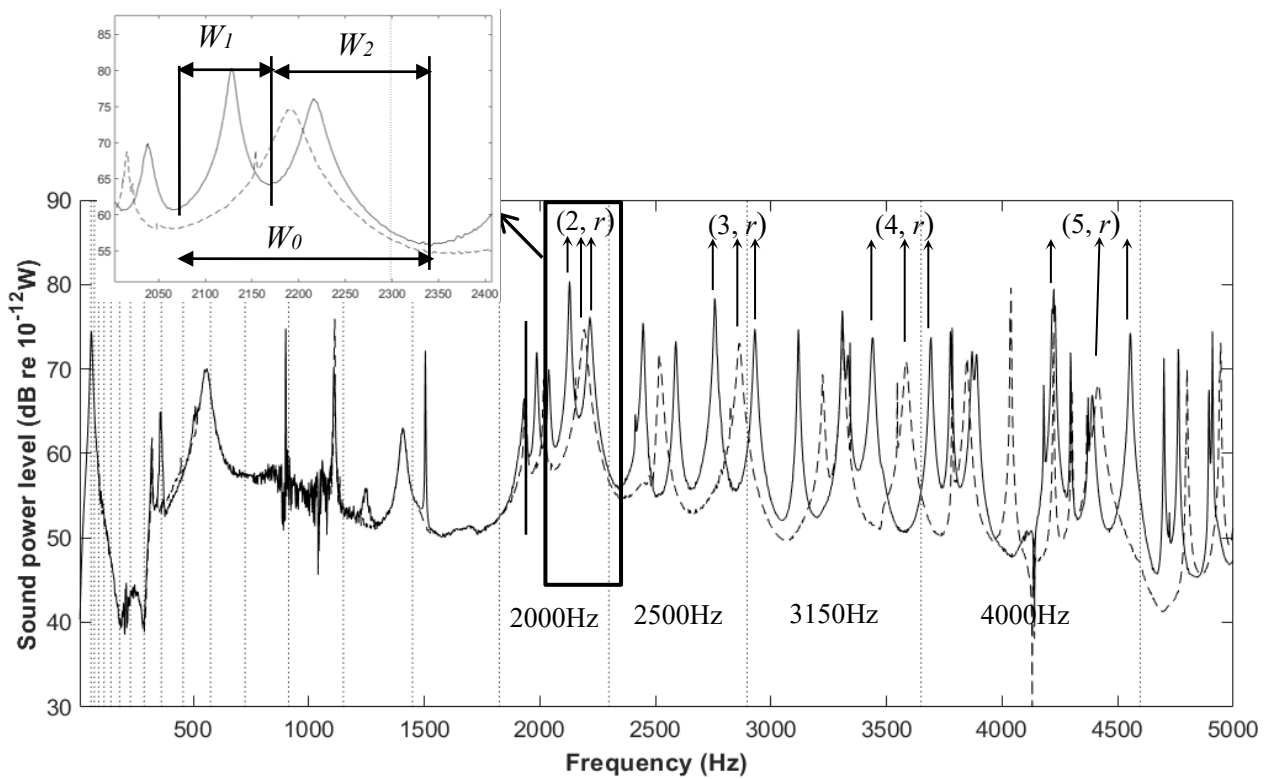


Fig. 13 Sound power level in narrow bands. —, wheelset rotation considered; ---, wheelset rotation not considered. (The vertical dotted lines indicate the boundaries of one-third octave bands).

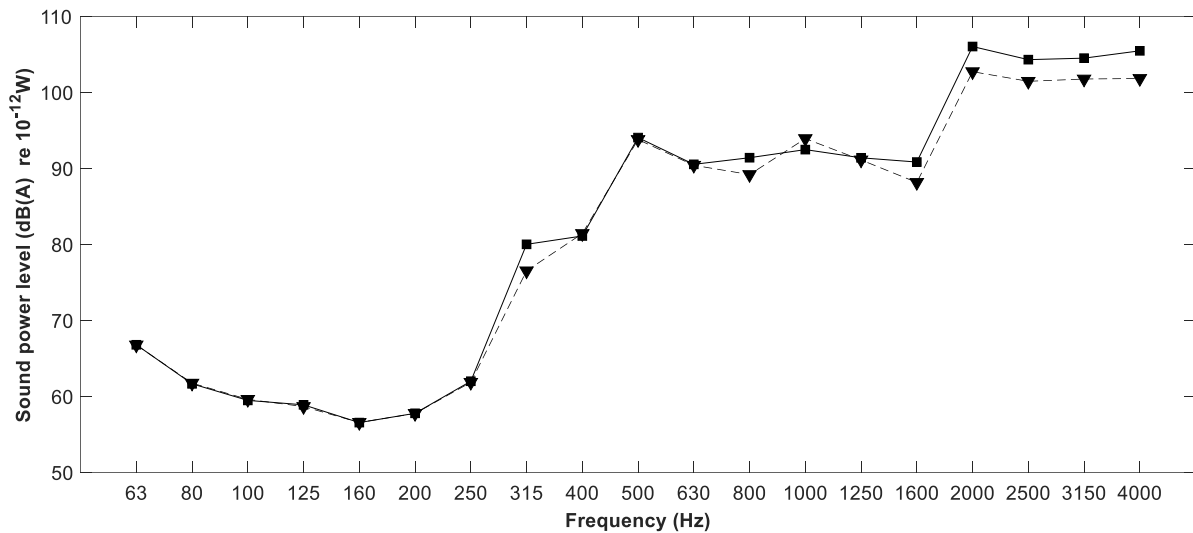


Fig. 14 Sound power level (A-weighted) in 1/3 octave bands. ■, wheelset rotation considered; ▼, wheelset rotation not considered.

A number of observations can be made. First, for frequencies below about 1600 Hz, wheelset rotation has insignificant effect on the predicted sound power. There are two reasons for this: (a) for those frequencies, the vertical wheel/rail force is mainly determined by the track and the contact spring, and therefore, wheelset rotation does not change the wheel/rail force significantly; and (b) the modes of the wheelset in this frequency range are less affected by wheelset rotation. Second, wheelset rotation can bring a peak in sound power from one 1/3 octave band to another, for example the higher of the two peaks associated with the $(3, r)$ and $(4, r)$ modes. Third, for frequencies above about 1600 Hz, the predicted sound power can be up to about 3 dB too low if wheelset rotation is ignored. The first two observations are quite easy to understand, but the third one deserves some discussion.

For frequencies above 1600 Hz, the peaks in the sound power are associated with the radial modes of the wheelset, as indicated in Fig. 13. A peak in the sound power is split into two peaks by wheelset rotation, one at a lower frequency and the other at a higher frequency, and the magnitudes at these two peaks are greater than for the one without wheelset rotation. The increase in the height of the peaks can be explained as follows.

It has been explained in Section 4.1 that the vertical wheel-rail force around the radial modal frequencies can be calculated by just using the vertical receptances of the wheelset, track and contact spring. The vertical receptance of the rotating wheelset, that of the nonrotating wheelset and that of the contact spring are shown in Fig. 15 for frequencies around mode $(2, r)$. The track receptance can be neglected at these frequencies as its magnitude is much lower than the other two receptances. For the case without wheelset rotation, the receptance has a peak at the wheelset natural frequency, 2154 Hz (denoted by ω_p) and an anti-resonance at 2320 Hz. Between these two frequencies, the phase

difference between the receptances of the contact spring and the wheelset is close to π , i.e. these two receptances are out of phase with one another. In this frequency range, the receptance magnitudes of the wheelset and the contact spring have an intersection at a frequency ω_c . At this frequency, the real parts of the receptances of the wheelset d_W and contact spring d_C nearly cancel each other, making the magnitude of the sum $d_W(\omega) + d_R(\omega) + d_C(\omega)$ (that of the track d_R being small) have a minimum and the wheel-rail force a maximum which is given by

$$|P_{VV}(\omega_c)| = \frac{|z(\omega_c)|}{|d_W(\omega_c) + d_R(\omega_c) + d_C(\omega_c)|} \approx \frac{|z(\omega_c)|}{|\text{Im}(d_R(\omega_c))|}. \quad (13)$$

This peak in the wheel/rail force generates a peak in the radiated sound power. If wheelset rotation is considered, the resonance frequency ω_p is split into two, ω_{p1} and ω_{p2} , which have a smaller magnitude; the intersection frequency ω_c is also split into two, ω_{c1} and ω_{c2} . The wheel/rail force at ω_{c1} and ω_{c2} is given by

$$|P_{VV}(\omega_{c1})| \approx \frac{|z(\omega_{c1})|}{|\text{Im}(d_R(\omega_{c1}))|}, \quad |P_{VV}(\omega_{c2})| \approx \frac{|z(\omega_{c2})|}{|\text{Im}(d_R(\omega_{c2}))|} \quad (14)$$

For a relatively flat roughness spectrum, it can be assumed that $|z(\omega_c)| \approx |z(\omega_{c1})| \approx |z(\omega_{c2})|$ and $\text{Im}(\alpha_R(\omega_c)) \approx \text{Im}(\alpha_R(\omega_{c1})) \approx \text{Im}(\alpha_R(\omega_{c2}))$. Thus, from Eqs. (13) and (14), the forces in each case are very similar, $|P_{VV}(\omega_c)| \approx |P_{VV}(\omega_{c1})| \approx |P_{VV}(\omega_{c2})|$. Now, with wheelset rotation, the intersection frequency is closer to the associated resonance frequency, and from Fig. 12 the sound power for a unit force will increase. Consequently, the sound power at the intersection frequency will be higher than it would be if wheelset rotation is neglected. The corresponding frequencies and peak sound power levels are summarized in Table 5. In addition, from Fig. 13, the bandwidth of the pairs of peaks in the rotating case is smaller than the bandwidth of the original peaks. Hence, the bandwidth also needs to be taken into account. Integrating the sound power over the frequency range of the peaks, the total sound power associated with each peak is also listed in Table 5. Although the bandwidth of the bifurcated peaks is smaller, the backward wave peak still contains more energy than the original peak, and the energy contained in the forward wave peak is comparable that of the original peak. The combined energy of the two will be 3.2 dB higher than the original peak energy. In summary, the reason for the difference at high frequencies is that each resonance frequency becomes two, and the apparent damping introduced at wheel/track coupled resonances becomes smaller after considering the rotation.

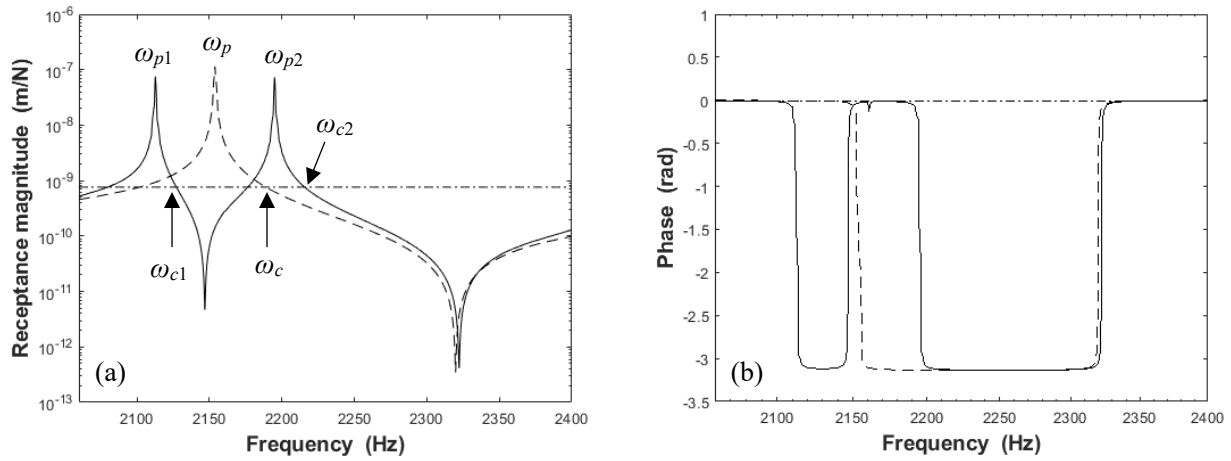


Fig. 15 Vertical receptances at the wheel/rail contact point. (a) Magnitude, (b) Phase; —, non-rotating wheelset; ---, rotating wheelset; - • -, contact spring.

Table 5 The radiation of rotating/ non-rotating wheelset at resonance and coupled resonance frequency for mode (2, r)

		Frequency (Hz)	Peak sound power level (dB)	Total sound power level (dB)
Non-rotating wheelset	Resonance ω_p	2153.5	\	\
	Intersection ω_c	2192.1 (+38.6)	74.9	100.8
Rotating wheelset (backward wave)	Resonance ω_{p1}	2112.7	\	\
	Intersection ω_{c1}	2130.0 (+17.3)	79.9 (+5.0)	101.6 (+0.8)
Rotating wheelset (forward wave)	Resonance ω_{p2}	2195.0	\	\
	Intersection ω_{c2}	2218.1 (+23.1)	76.1 (+1.2)	100.3 (-0.5)

4.4 Effect of superstructure

The effect of the superstructure on the wheelset noise is considered in this section. A comparison of the sound power radiated by the wheelset is shown and Fig. 16 between cases with (the benchmark) and without the superstructure. In both cases the vertical and lateral interaction and wheelset rotation are included. The A-weighted sound power levels in 1/3 octave bands are compared in Fig. 17.

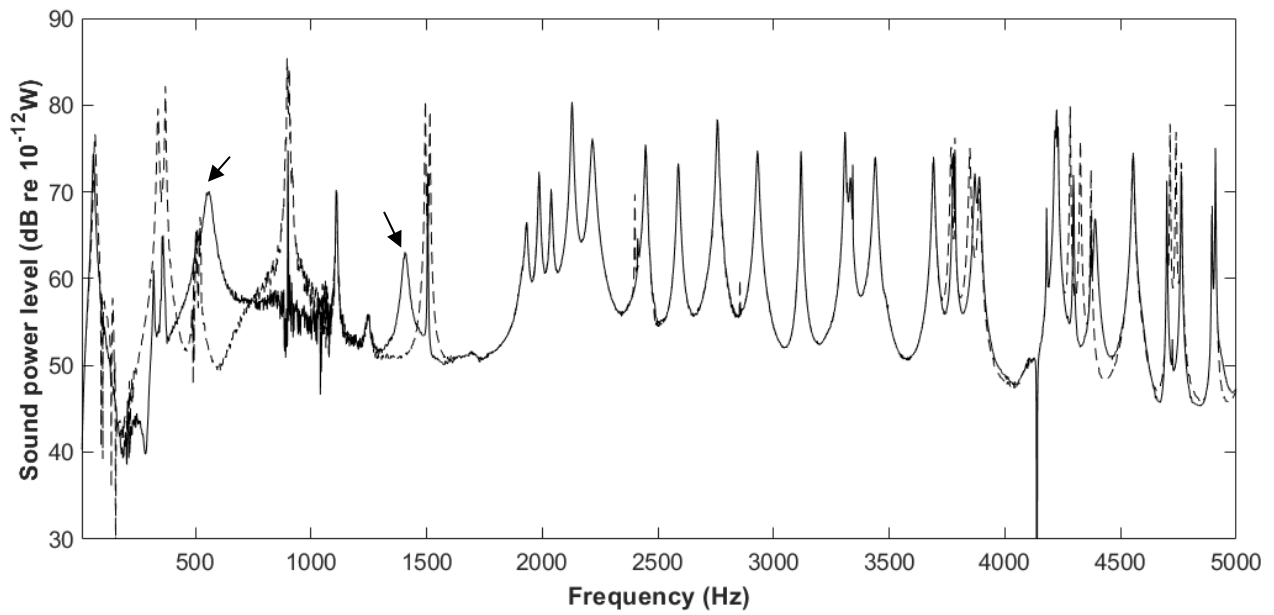


Fig. 16 Narrow band sound power level radiated by the wheelset. —, with superstructure; - - -, without superstructure.

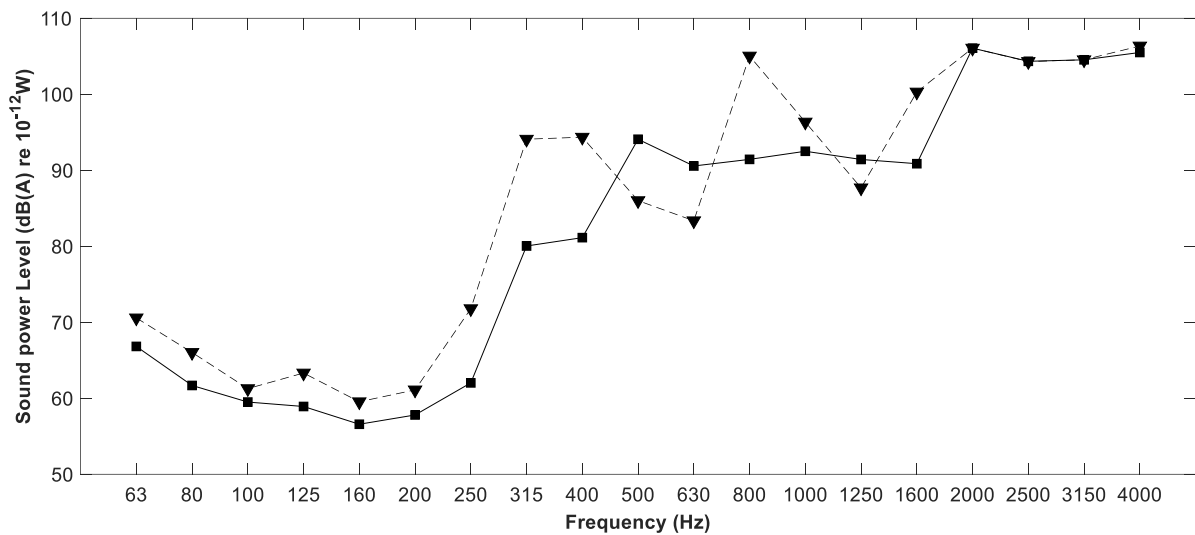


Fig. 17 1/3 octave band sound power level (A-weighted) radiated by the wheelset. ■, with superstructure ; ▼, without superstructure.

From Fig. 16, it is found that inclusion of the superstructure will suppress some peaks in the sound power. However, in the 1/3 octave band spectra in Fig. 17, the presence of the superstructure makes differences only for frequencies below 1600 Hz since the acoustic radiation in the high frequency region is mainly dominated by the radial modes of the wheelset. The suppressed peaks occur at 338 Hz, 371 Hz, 1494 Hz, 1514 Hz, 4282 Hz, 4326 Hz, etc., corresponding to mode shapes with large vertical vibration at both ends of the axle that are affected by the damping introduced by coupling between the superstructure and the wheelset. Moreover, with the inclusion of the wheelset superstructure, there are new peaks at 558 Hz and 1405 Hz emerging, mainly because the coupling

between the wheelset and the superstructure introduces new vibration modes to the coupling structure. The two vibration modes, in which the vertical vibration at ends of the axle and the vertical vibration of the axlebox are in phase and reverse respectively, are shown in Fig. 18. This is because the bending vibration of the axle can be equated to a mass-spring system over a range of frequencies and forms a two-degree-of-freedom system with the axlebox, so that the two peak frequencies of 558 Hz and 1405 Hz are distributed on either side of the natural frequency (about 790 Hz) of the single-degree-of-freedom mass-spring system formed by the axlebox and bearing. These peaks do not split into two because they are associated with the superstructure which does not rotate.

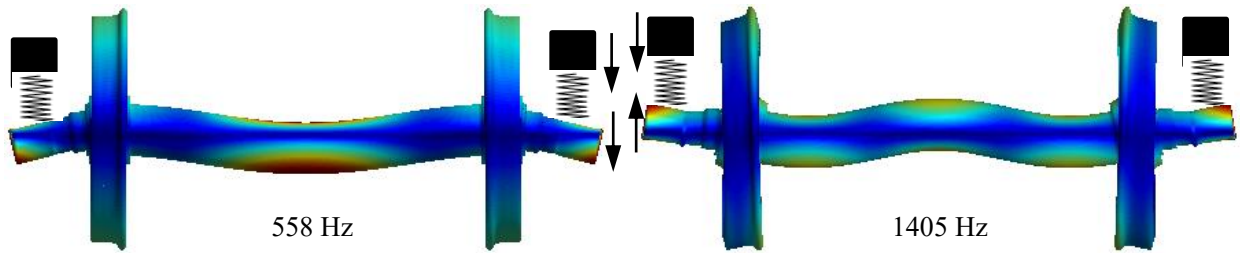


Fig. 18 Vibration modes of coupling structure of the wheelset and the superstructure

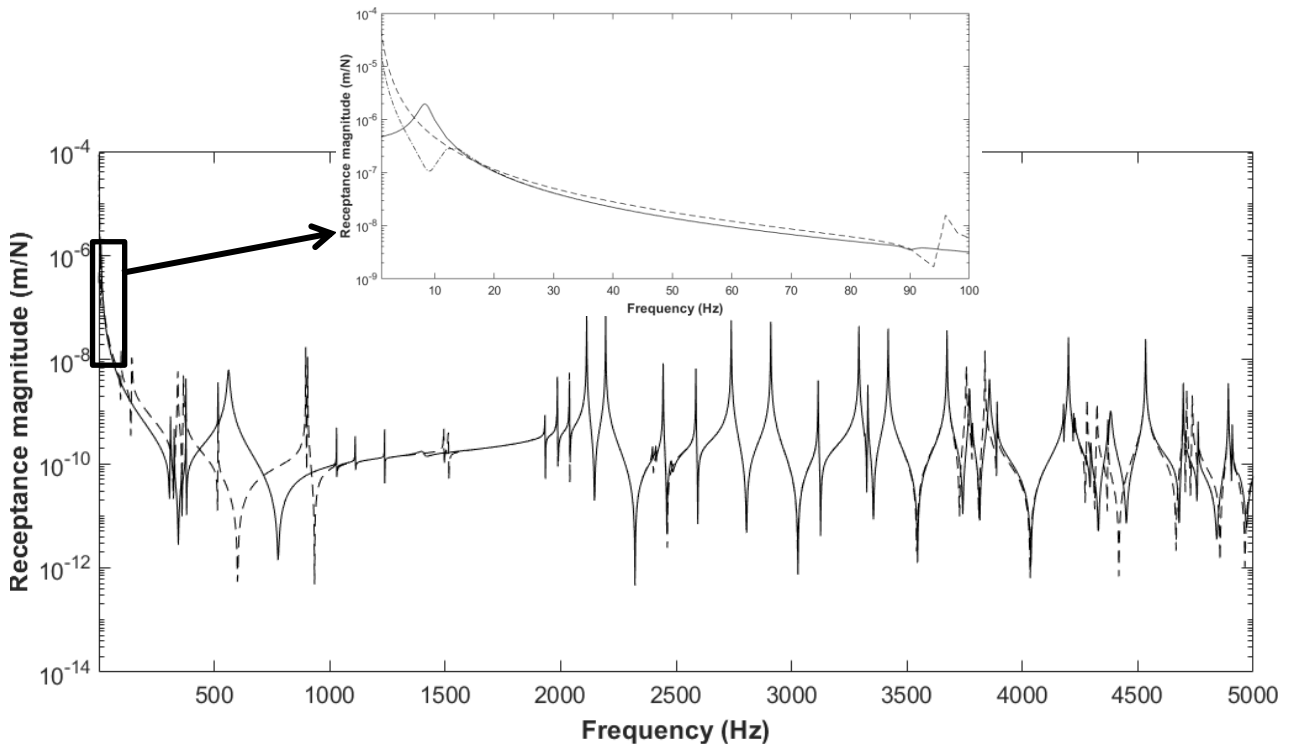


Fig. 19 Vertical receptance magnitude of wheelset at the wheel/rail contact point. —, with superstructure; — • —, without superstructure; - • -, only with axle box and rotary arm.

These phenomena are reflected in Fig. 17, which shows that inclusion of the superstructure leads to a significant reduction in radiated noise in the 1/3 octave bands of 800 Hz, 1000 Hz, 1600 Hz and bands below 400 Hz, and an increase in the 1/3 octave bands of 500 Hz, 630 Hz and 1250 Hz.

The vertical receptance magnitude of the wheelset with superstructure, without superstructure, or with only the axle box and rotary arm are compared in Fig. 19. The suppressed or emerging sound power peaks observed in Fig. 16 also manifest themselves in the vertical receptance. The receptance including the full superstructure model is almost identical to the one including only the axlebox and rotary arm, except below 20 Hz which is not important for the acoustic radiation. Hence, it is sufficient to include only the axle box and rotary arm to calculate the receptance and radiation from the wheelset.

4.5 Effect of incoherent excitation at the two wheel/rail contacts

From Eq. (8), when Ψ is equal to π , the left and right wheel/rail forces will be anti-symmetric. The sound power due to the symmetrical and anti-symmetrical roughness (they have the same magnitude) are shown in Fig. 20. (The calculations in this section take into account the rotation of the wheelset and the presence of the superstructure as described above.)

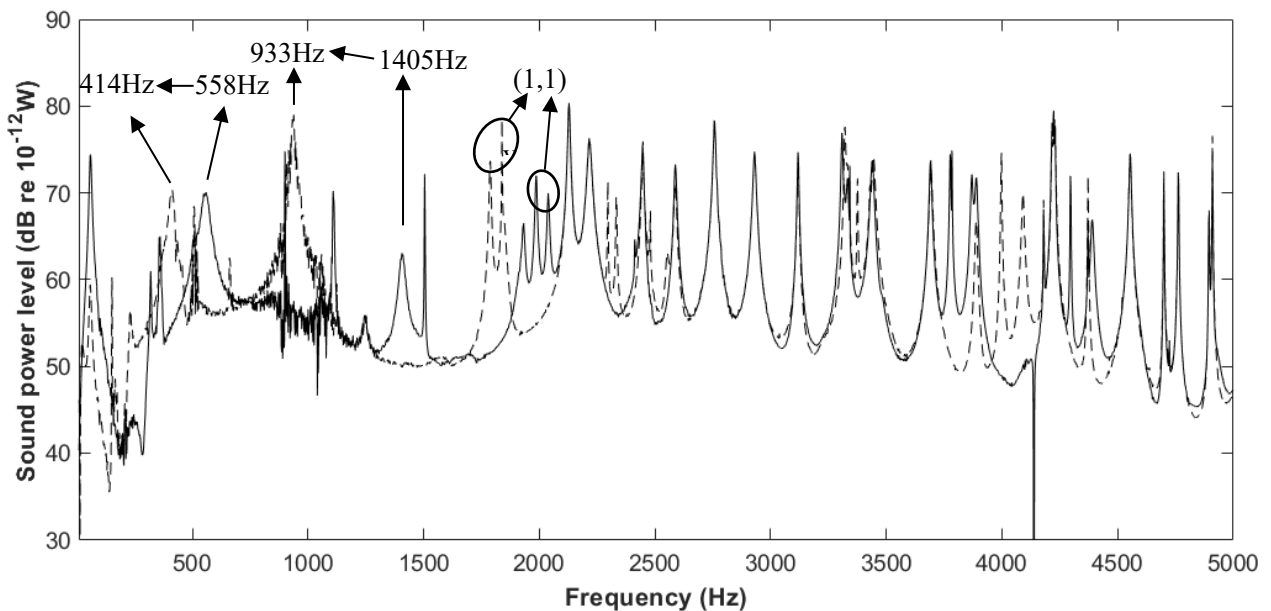


Fig. 20 Sound power level in narrow band radiated by the wheelset. —, due to symmetrical roughness; ---, due to anti-symmetrical roughness.

From Fig. 20, the sound power peak at about 67 Hz due to the so-called P2 wheel/rail force is greatly reduced. This is because at low frequencies, symmetrical excitation causes translational motion and antisymmetrical excitation causes side-roll motion, and the acoustic radiation efficiency caused by the two motions can be different.

In addition, in Fig. 20, there are some different peaks present in the sound power curve for the anti-symmetric excitation, which correspond to anti-symmetrical wheelset modes. A beam generally has alternate symmetric and antisymmetric modes and the same is true for bending modes of the wheelset. However, for $n \geq 2$, the axle transmits virtually no vibration, so symmetric and antisymmetric

modes have identical modal frequencies. Therefore, the results for the two cases only differ from each other for the modes with $n=0$ and $n=1$. The (1, 1) modes are highlighted in Fig. 20 by way of example. There are two modes (1, 1) occurring at different frequencies which occur separately for symmetric and anti-symmetric excitation, in each case as twin peaks. Same as (1, 1) modes, the peaks at 558 Hz and 414 Hz, 1405 Hz and 933 Hz are also two sets of twin frequencies.

Fig. 21 presents a comparison of the sound power due to symmetrical excitation from Eq. (7) and incoherent excitation from Eq. (10). These results are shown in Fig. 22 in 1/3 octave band form. Considering the incoherent roughness excitation, the radiated noise in the frequency region below 160 Hz is reduced compared with symmetrical excitation, the radiated noise between 160 Hz and 1600 Hz is generally increased, but the overall A-weighted level is changed from 111.5 dB(A) to 111.7 dB(A) because the noise remains largely unchanged above 1600 Hz (where modes with $n \geq 2$ dominate).

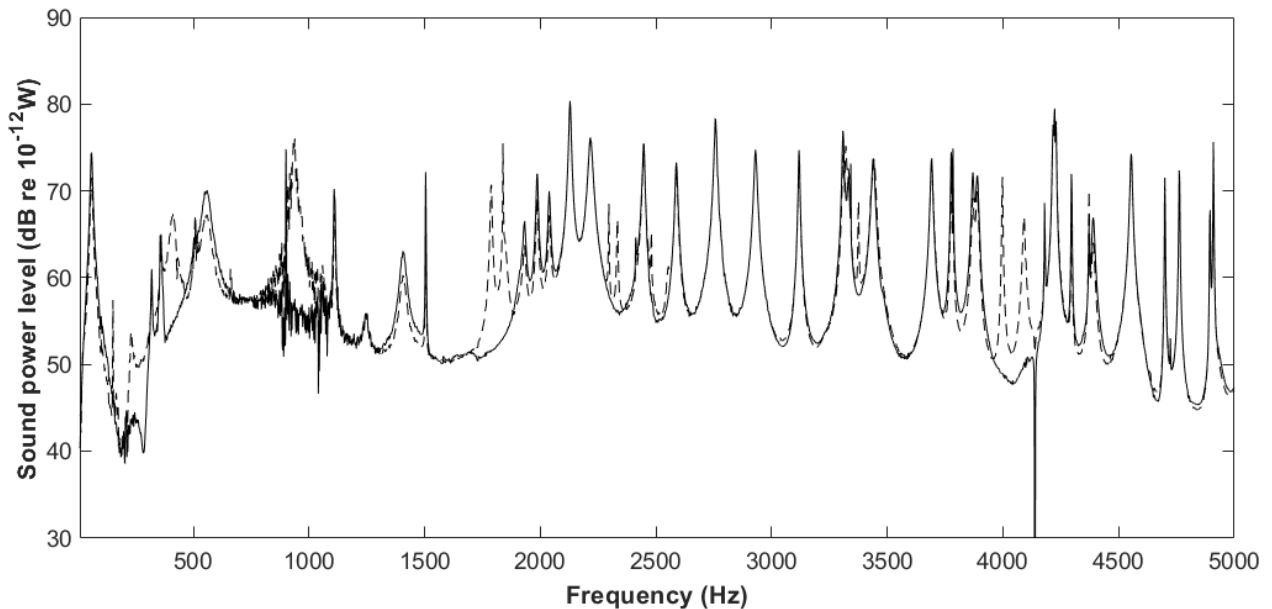


Fig. 21 Sound power level in narrow band radiated by the wheelset. —, due to excitation by symmetrical roughness ($\Psi = 0$); ---, due to incoherent excitation of the two wheels.

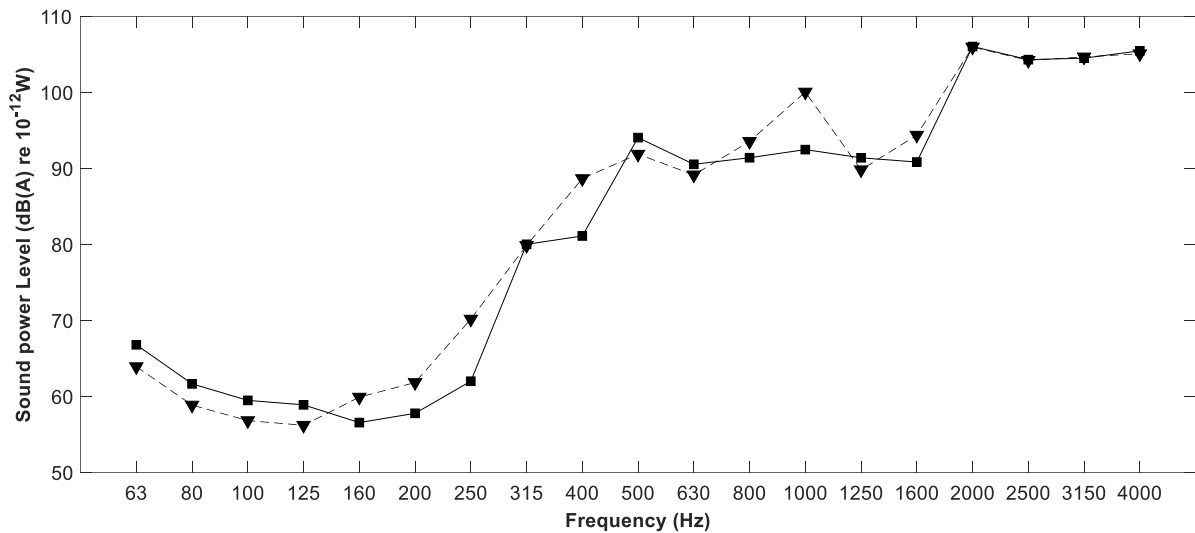


Fig. 22 Sound power level in 1/3 octave bands (A-weighted) radiated by the wheelset. ■, due to excitation by symmetrical roughness ($\Psi = 0$); ▼, due to incoherent excitation of the two wheels.

4.6 The sound power contributions from the two wheels and the axle

On the basis of the calculation method presented in this paper, the sound power radiated from the axle and the two wheels can be distinguished. The sound power from these components, for incoherent excitation on the two wheels, is shown in Fig. 23. The noise radiated by the axle cannot be discounted in much of the frequency range up to 1000 Hz. However, the overall A-weighted sound power level due to the wheels is 111.3 dB(A) and that due to the axle is 100.8 dB(A), which can therefore be considered negligible.

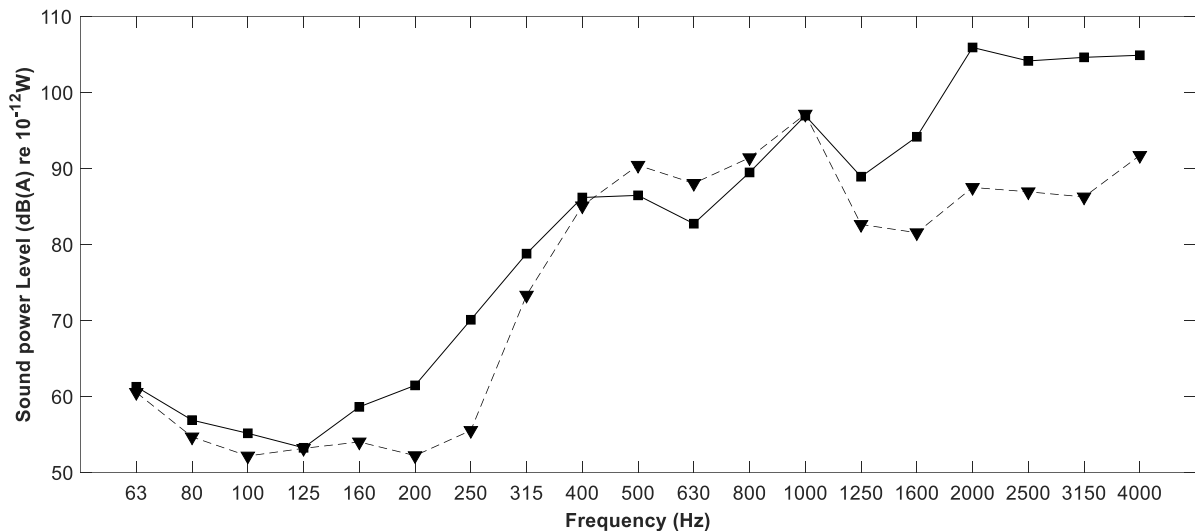


Fig. 23 Sound power level in 1/3 octave bands (A-weighted) radiated by, ■, left wheel and right wheel; ▼, axle

5. Conclusions

The sound power radiated by a wheelset is obtained by using the finite element and boundary

element methods. Use is made of the axi-symmetry of the wheelset to allow the solution to be obtained in terms of a Fourier series in the circumferential direction. The effect of various modelling assumptions is investigated to determine their influence on the wheel/rail force and wheelset-radiated sound power. The following conclusions are drawn:

(1) If the wheelset receptance takes into account the high-speed rotation, the moving-roughness approach is sufficient for calculating the sound radiation from the wheelset. However, for the track response and radiation it is likely to be more important to include the moving-wheel excitation.

(2) As stated in Ref. [1], it is necessary to include coupling between the wheel and rail in the lateral direction as well as the vertical one. Considering vertical coupling alone will greatly overestimate the contribution of the axial modes of the wheel, and thus the overall wheelset radiated noise.

(3) If the rotation of the wheelset is not considered, the radiated noise of the wheelset may be underestimated by up to 3 dB at frequencies above about 2000 Hz, mainly because there are twice as many peaks and the apparent damping introduced by the wheel/rail coupling is smaller for the case with rotation.

(4) When the superstructure is included, some radiation peaks due to modes with large vertical vibration at both ends of the axle are suppressed, thus reducing the overall sound power at frequencies below 2000 Hz. It may be sufficient to include only the bearings and axleboxes to calculate the radiation from wheelset.

(5) Compared with symmetric excitation of the wheelset, introducing the more realistic incoherent excitation of the left and right wheel/rail contacts will greatly affect the radiated noise at frequencies below 2000 Hz. However, the effect on the overall noise level is small.

(6) The sound power from the axle is significant for frequencies below 1000 Hz, but it has little influence on the overall sound power of the wheelset.

The quantitative impact of these assumptions on sound power radiated by wheelset is summarised in Table 6, in which ‘+’ represents an overestimation of sound power and ‘-’ represents an underestimation of sound power if the factor defined in the first column is assumed to be not considered.

Table 6 Effects of modelling assumptions on sound power radiated by the wheelset

Factors	Over- or underestimation in	
	Overall A-weighted sound power level	1/3-octave band A-weighted sound power level (the

		maximum of all the bands)
Lateral wheel/rail interaction	+4.8 dB(A)	500 Hz, +15.2 dB(A)
Wheelset rotation	-2.9 dB(A)	2000 Hz, -3.3 dB(A)
Superstructure of wheelset	+1.3 dB(A)	315 Hz, +14 dB(A)
Incoherence of left and right roughness	-0.2 dB(A)	1000 Hz, -6.6 dB(A)
Inclusion of sound power from axle	-0.4 dB(A)	630 Hz, -6.4dB(A)

Acknowledgments

This work is funded by the National Natural Science Foundation of China (U1834201), the National Key R&D Program of China (2016YFE0205200), Sichuan Science and Technology Program (2020YJ0076), and the Fundamental Research Funds for the Central Universities (2682020CX35).

References

- [1] D. J. Thompson, *Railway noise and vibration: mechanisms, modelling and means of control*, Elsevier, Oxford, 2009.
- [2] P. J. Remington, Wheel/rail noise, Part I: characterization of the wheel/rail dynamic system, *J. Sound Vib.* 46 (3) (1976) 359-379.
- [3] P. J. Remington, Wheel/rail noise, Part IV: rolling noise, *J. Sound Vib.* 46 (3) (1976) 419-436.
- [4] E. Schneider, K. Popp, H. Irretier, Noise generation in railway wheels due to rail-wheel contact force, *J. Sound Vib.* 120 (1986) 227-244.
- [5] D. J. Thompson, Wheel/rail noise generation, Part II: Wheel vibration, *J. Sound Vib.* 161 (1993) 401-419.
- [6] D. J. Thompson, C. J. C. Jones, Sound radiation from a vibrating railway wheel, *J. Sound Vib.* 253 (2) (2002) 401-419.
- [7] D. J. Thompson, B. Hemsworth, N. Vincent, Experimental validation of the TWINS prediction program for rolling noise, Part I: description of the model and method, *J. Sound Vib.* 193 (1) (1996) 123-135.
- [8] C. J. C. Jones, D. J. Thompson, Extended validation of a theoretical model for railway rolling noise using novel wheel and track designs, *J. Sound Vib.* 267 (2003) 509-522.
- [9] J. Han, S. Zhong, X. Zhou, X. Xiao, G. Zhao, X. Jin, Time-domain model for wheel/rail noise analysis at high operation speed, *J. Zhejiang Univ-Sc. A.* 18 (8) (2017) 593-602.

- [10] D. J. Thompson, Wheel/rail noise generation, Part V: Inclusion of wheel rotation, *J. Sound Vib.* 161 (1993) 467-482.
- [11] J. Fayos, L. Baeza, F. D. Denia, J. E. Tarancon, An Eulerian coordinate-based method for analysing the structural vibrations of a solid of revolution rotating about its main axis, *J. Sound Vib.* 306 (2007) 618-635.
- [12] P. T. Torstensson, J. C. O. Nielsen, L. Baeza, Dynamic train-track interaction at high vehicle speeds-Modelling of wheelset dynamics and wheel rotation, *J. Sound Vib.* 330 (2011) 5309-5321.
- [13] L. Baeza, J. G. Navarro, D. J. Thompson, J. Monterde, Eulerian models of the rotating flexible wheelset for high frequency railway dynamics, *J. Sound Vib.* 449 (2019) 300-314.
- [14] X. Sheng, Y. Liu, X. Zhou, The response of a high-speed train wheel to a harmonic wheel-rail force, *Journal of Physics: Conference Series*, Southampton, 744 (2016) 012145.
- [15] T. Zhong, G. Cheng, X. Sheng, X. Zhan, L. Zhou, J. Kai, Vibration and sound radiation of a rotating train wheel subject to a vertical harmonic wheel/rail force, *J. Mod. Trans.* 26 (2) (2018) 81-95.
- [16] X. Sheng, G. Cheng, D. J. Thompson, Modelling wheel/rail rolling noise for a high-speed train running along an infinitely long periodic slab track, *J. Acoust. Soc. Am.* 148 (1) (2020) 174-190.
- [17] X. Sheng, Y. Peng, X. Xiao, Boundary integral equations for sound radiation from a harmonically vibrating body moving uniformly in a free space, *J. Acoust. Soc. Am.* 146(6) (2019) 4493-4506.
- [18] X. Sheng, C. J. C. Jones, D. J. Thompson, Responses of infinite periodic structures to moving or stationary harmonic loads, *J. Sound Vib.* 282 (2005) 125-149.
- [19] T. X. Wu, D. J. Thompson, Application of a multiple-beam model for lateral vibration analysis of a discretely supported rail at high frequencies, *J. Acoust. Soc. Am.* 108 (3) (2000) 1341-1344.
- [20] X. Sheng, M. Li, C. J. C. Jones, D. J. Thompson, Using the Fourier-series approach to study interactions between moving wheels and a periodically supported rail, *J. Sound Vib.* 303 (2007) 873-894.
- [21] X. Sheng, T. Zhong, Y. Li, Vibration and sound radiation of slab high-speed railway tracks subject to a moving harmonic load, *J. Sound Vib.* 395 (2017) 160-186.
- [22] X. Sheng, D. J. Thompson, C. J. C Jones, Modelling rail roughness growth on tangent tracks, ISVR Technical Memorandum, University of Southampton (2004).

- [23]ISO 3095: Acoustics - Railway applications - Measurement of noise emitted by railbound vehicles, International Standards Organization (2013).
- [24]ORE B 176 Bogies with steered or steering wheelsets. Report No. 1: specifications and preliminary studies. Vol. 2, Specification for a bogie with improved curving characteristics, Utrecht: ORE (1989).
- [25]X. Sheng, M. H. Li, Propagation constants of railway tracks as a periodic structure, *J. Sound Vib.* 299 (2007) 1114-1123.
- [26]S. Zhang, G. Cheng, X. Sheng, D. J. Thompson, Dynamic wheel-rail interaction at high speed based on time-domain moving Green's functions, *J. Sound Vib.* 488 (2020) 115632.
- [27]E. Ntotsios, D. J. Thompson, M. F. M. Hussein, The effect of track load correlation on ground-borne vibration from railways, *J. Sound Vib.* 402 (2017) 142–163.